

*Electronic Supplementary Information (ESI) for*

**Construction of highly efficient new binder-free bimetallic Metal-Organic framework symmetric supercapacitors: considering surface statistical and morphological analyses**

Fatemeh Ghamari<sup>1</sup>, Davood Raoufi<sup>1\*</sup>, Saber Alizadeh<sup>2</sup>, Jalal Arjomandi<sup>3</sup>, Davood Nematollahi<sup>2</sup>

<sup>1</sup>Department of Physics, Faculty of science, Bu-Ali Sina University, PO Box 65174, Hamedan, Iran

<sup>2</sup>Faculty of Chemistry, Bu-Ali-Sina University, 38695-65178 Hamedan, Iran

<sup>3</sup>Department of Physical Chemistry, Faculty of Chemistry, Bu-Ali Sina University, 65178 Hamedan, Iran,

\*To whom correspondence should be addressed, E-mails: [raoufi@basu.ac.ir](mailto:raoufi@basu.ac.ir) and [d\\_raoufi@yahoo.com](mailto:d_raoufi@yahoo.com)

---

\* [raoufi@basu.ac.ir](mailto:raoufi@basu.ac.ir) and [d\\_raoufi@yahoo.com](mailto:d_raoufi@yahoo.com)

## Table of Contents:

<b>Note S1: Experimental section</b> .....	5
S1.1 Chemicals.....	5
S1.2 Preparation of hierarchically porous metal organic framework electrodes .....	5
S1.2.1. Construction of (Co, Zn, Ni)-BTC m-MMOF modified electrodes .....	5
S1.2.2. Construction of (Ni/Co) and (Ni/Zn)-BTC bi-MMOF modified electrodes.	6
S1.3 Apparatus and instrument .....	6
S1.4 Electrochemical investigations .....	7
S1.4.1 Electrochemical studies in a three-electrode setup .....	7
S1.4.2 Electrochemical studies in a two-electrode setup .....	7
S1.4.3 Evaluation of the electrochemical parameters .....	8
<b>Figure S1.</b> X-ray diffraction patterns of the synthesized MOFs electrodes .....	9
<b>Figure S2.</b> FT-IR spectrum recorded for the synthesized MOFs. ....	10
<b>Figure S3.</b> FE-SEM images of the Ni-foam substrate and the MMOF modified electrodes in different magnifications: (A) Ni-foam substrate, (B) Ni/Co-BTC, (C) Ni/Zn-BTC, (D) Ni-BTC, (E) Zn-BTC, and (F) Co-BTC electrodes. ....	11
<b>Figure S4.</b> EDX spectrum of (A) Ni/Co-BTC, (B) Ni/Zn-BTC, (C) Ni-BTC, (D) Zn-BTC, (E) Co-BTC electrodes, elemental mapping of all the elements present in the electrodes, and overall elemental mapping images of these compounds. ....	16
<b>Figure S5.</b> XRD pattern of MOF//Ni-foam electrode and the representation of Ni/Co-BTC and Ni-foam corresponding peaks.....	17
<b>Figure S6.</b> XPS high-resolution spectra: (a <sub>1</sub> , and b <sub>1</sub> ) C 1s, and (a <sub>2</sub> , and b <sub>2</sub> ) O 1s for (a) Co/Ni-BTC and (b) Ni/Zn-BTC MOF electrodes. ....	18
<b>Note S2: Statistical and stereometric analyses</b> .....	19
S 2.1. The definition of statistical and stereometric parameters .....	21
S2.2 The definition of the surface segmentation parameters .....	22
S2.3 The description of fractal dimension calculating method.....	23
<b>Figure S7.</b> (a <sub>1</sub> -e <sub>1</sub> ) represent the areal material ratio curves describing functional stratified surface parameters, (a <sub>2</sub> -e <sub>2</sub> ) represent the motifs of significant shapes thorough the watershed segmentation algorithm, and (a <sub>3</sub> -e <sub>3</sub> ) reveal the surface furrows of AFM images with 1 $\mu$ m $\times$ 1 $\mu$ m scanning square areas for the MOF electrodes: (a) Ni/Co-BTC, (b) Ni/Zn-BTC, (c) Ni-BTC, (d) Zn-BTC, and (e) Co-BTC. ....	24

<b>Table S1.</b> The basic features of the height quantities distribution and functional parameters (stratified surfaces) derived from the Bearing Area Curve (BAC) of the AFM images of m-MMOF and bi-MMOF, for scanning square areas of $1\mu\text{m} \times 1\mu\text{m}$ . .....	25
<b>Table S2.</b> Parameter values of shapes resulting from surface segmentation using the watershed segmentation algorithm of analyzing samples. ....	26
<b>Table S3.</b> The furrows parameters of mono-metallic and mix-metallic MOF, for scanning square areas of $1\mu\text{m} \times 1\mu\text{m}$ . ....	27
<b>Figure S8.</b> Logarithmic plot of number of enclosing boxes ( $N(\varepsilon)$ ) versus the scale of analysis ( $\varepsilon$ ) from the box-counting method for (A) Ni/Co-BTC, (B) Ni/Zn-BTC, (C) Ni-BTC, (D) Zn-BTC, and (E) Co-BTC. ....	28
<b>Figure S9.</b> Cartesian representation of texture directions for the surfaces of the MOF electrodes: (A) Ni/Co-BTC, (B) Ni/Zn-BTC, (C) Ni-BTC, (D) Zn-BTC, and (E) Co-BTC .....	29
<b>Table S4.</b> Fractal dimensions determined via the cube counting method and the texture aspect ratio ( $S_{tr}$ ) or isotropy and the texture direction of mono-fractal surfaces derived from AFM images of m-MMOF and bi-MMOF electrodes.....	30
<b>Note S3. Quantitative description of the EIS measurements</b> .....	31
<b>Table S5.</b> The values of elements for equivalent circuits (the inset of Fig. 4A) fitted to the Nyquist diagrams of Fig. 4A and the corresponding relative errors .....	32
<b>Figure S10.</b> ( $a_1$ , and $b_1$ ) three-electrode CVs curves of Ni/Co-BTC and Ni/Zn-BTC electrodes at different scan rates, ( $c_1$ ) a comparison between the CV curves of bi-MMOF electrodes at a scan rate of $40\text{ mV s}^{-1}$ and, ( $d_1$ ) $C_s$ of bi-MMOF electrodes at various scan rates; ( $a_2$ , and $b_2$ ) three-electrode GCD curves of Ni/Co-BTC and Ni/Zn-BTC electrodes at different currents, ( $c_2$ ) a comparison between the GCD curves of bi-MMOF electrodes at $2.5\text{ A g}^{-1}$ , and ( $d_2$ ) $C_s$ of bi-MMOF electrodes as a function of current density. ....	34
<b>Figure S11.</b> (A) Three-electrode CV curves of Ni-MOF at different scan rates, (B) GCD curves of Ni-BTC electrode at different current densities. ....	35
<b>Figure S12.</b> ( $a_1$ , and $b_1$ ) Three-electrode CV curves of Zn-MOF and Co-MOF at different scan rates, ( $a_2$ , and $b_2$ ) GCD curves of Zn-BTC and Co-BTC electrodes at different current densities, respectively. ....	36
<b>Figure S13.</b> The Randles–Sevcik plot of the peak current vs. the square root of the scan rate for Ni/Co-BTC and Ni/Zn-BTC electrodes.....	37
<b>Figure S14.</b> (A) Cycle-life stability of the Ni/Co-BTC and Ni/Zn-BTC electrodes at $30.0\text{ A g}^{-1}$ for 5000 cycles and (B) comparing the first cycle with the last cycle of capacitance retention test for Ni/Co-BTC electrode. ....	38

<b>Figure S15.</b> Cycle-life stability of the Ni -BTC electrode at 30.0 A g <sup>-1</sup> for 5000 cycles.....	39
<b>Table S6.</b> Comparison of the specific capacity of current work to the specific capacity of MOF and MOF-derived material reported in the previous literature. ....	40
<b>Table S7.</b> The main performance parameters for the Ni/Co-MOF//Ni/Co-MOF symmetric supercapacitor.....	41
<b>Table S8.</b> The main performance parameters for the Ni/Zn-MOF//Ni/Zn-MOF symmetric supercapacitor.....	42
<b>References:</b> .....	43

## **Note S1: Experimental section**

### **S1.1 Chemicals**

Nickel (II) nitrate hexahydrate ( $\text{Ni}(\text{NO}_3)_2 \cdot 6\text{H}_2\text{O}$ ; 99%), zinc nitrate hexahydrate ( $\text{Zn}(\text{NO}_3)_2 \cdot 6\text{H}_2\text{O}$ ; 99%), and cobalt (II) nitrate hexahydrate ( $\text{Co}(\text{NO}_3)_2 \cdot 6\text{H}_2\text{O}$ ; 99%) as pro-analysis grade materials were procured from the Sigma-Aldrich Chemical Company. Also, Benzene-1, 3, 5-tricarboxylic acid ( $\text{H}_3\text{BTC}$ ; 95%), potassium hydrate ( $\text{KOH}$ ; 99%), and ethanol ( $\text{C}_2\text{H}_5\text{OH}$ ; 99%) as reagent-grade materials were provided through the Merck Company. The materials were utilized without extra purification as received. The used solutions were prepared with distillate water via a Millipore Milli-Q water purification instrument at room temperature and daily time.

### **S1.2 Preparation of hierarchically porous metal organic framework electrodes**

#### ***S1.2.1. Construction of (Co, Zn, Ni)-BTC m-MMOF modified electrodes***

The (Ni, Co, Zn)-BTC m-MMOFs modified electrodes were fabricated through a one-step facile hydrothermal route. In a typical process of Ni-BTC electrode construction, trimesic acid ( $\text{H}_3\text{BTC}$ ; 0.42 g) and nickel (II) nitrate hexahydrate ( $\text{Ni}(\text{NO}_3)_2 \cdot 6\text{H}_2\text{O}$ ; 0.92 g) were dissolved in ethanol (15 mL) and distilled water (15 mL), respectively, by vigorous magnetic stirring at room temperature for 15 minutes. Then, two primary precursors were added together and were stirred magnetically for 15 minutes. Afterward, the synthesis process was followed by transferring the resultant solution into an autoclave (composed of stainless steel with Teflon-lined and a volume of 120 ml). At the primary stage of synthesis, the cleaning procedure of a Ni-foam electrode (as a substrate) was followed through the ultrasonic instrument for 15 min in ethanol, acetone, and distilled water, respectively. Then, the Ni-foam electrode, with the dimension of  $10 \times 10$  mm was placed into the autoclave solution, and subsequently was heated at  $120^\circ\text{C}$  for 24 h., with the dimension of  $10 \times 10$  mm was placed into the autoclave solution, and subsequently was heated at  $120^\circ\text{C}$  for 24 h. To obtain the appropriate deposited crystal structure on the Ni-foam electrode the autoclave was slowly cooled. Finally, the modified electrodes were washed with ethanol and distilled water three times and aged for 10 h at  $80^\circ\text{C}$ . Similar processes were performed for the fabrication of Zn-BTC and Co-BTC modified electrodes by using the ( $\text{Zn}(\text{NO}_3)_2 \cdot 6\text{H}_2\text{O}$ ; 0.95 g) and ( $\text{Co}(\text{NO}_3)_2 \cdot 6\text{H}_2\text{O}$ ; 0.93 g) instead of nickel.

### ***S1.2.2. Construction of (Ni/Co) and (Ni/Zn)-BTC bi-MMOF modified electrodes***

According to the above-mentioned procedure, the Ni/Zn-BTC and Ni/Co-BTC bi-MMOF modified electrodes were fabricated through a one-step/one-pot and binder-free hydrothermal method. In the preparing process of Co/Ni-BTC electrode, both Ni (NO<sub>3</sub>)<sub>2</sub>.6H<sub>2</sub>O (0.46 g) and Co (NO<sub>3</sub>)<sub>2</sub>.6H<sub>2</sub>O (0.46 g) were added simultaneously to distilled water (15 mL), as solution A. Also, trimesic acid (H<sub>3</sub>BTC; 0.42 g) was dissolved in ethanol (15 mL) as solution B. Afterward, solution A was added to the solution B by a drop to a drop under stirred magnetically for 15 minutes. The resulted precursor transferred into the autoclave contained the Ni-foam electrode and was heated for 24 h at 120 °C. Finally, the modified electrodes were taken from the solution and were washed with ethanol and distilled water three times, and aged at 80 °C for 10 h. The same procedure was accomplished to prepare the Ni/Zn-BTC electrode by using the Zn (NO<sub>3</sub>)<sub>2</sub>.6H<sub>2</sub>O (0.47 g) instead of the Co (NO<sub>3</sub>)<sub>2</sub>.6H<sub>2</sub>O (Scheme 1).

### **S1.3 Apparatus and instrument**

For investigation of the modified electrodes, the following instruments were utilized. The crystallographic data were acquired via X-ray powder diffraction (XRD) technique by employing the (PANalytical, Inc. X'Pert Pro Multi-Functional Powder Diffractometer) equipped with the radiation of monochromatic Cu-K $\alpha$ 1 ( $\lambda=0.1542$ ) and the step width ( $2\theta=0.04^\circ$ ) for scanning. The transmission spectra via Fourier transform infrared (FT-IR) spectroscopy for the synthesized scratched materials were recorded through a Perkin Elmer FT-IRGX spectrometer in the range of 400- 4000 cm<sup>-1</sup> wave-numbers by KBr pellets. Surface morphological analysis of the modified electrodes was investigated with the Field-Emission Scanning Electron Microscopy (FE-SEM) using HITACHI S-4160 instrument, and Atomic Force Microscopy (AFM) at room temperature ( $297 \pm 1$  K) in the non-contact mode with scanning square areas of  $1\mu\text{m}\times 1\mu\text{m}$  and  $512\times 512$  pixels using BRUKER's AFM In., ICON apparatus, respectively. The processing of AFM images carried out via the Mountains Map® Premium software Ver. 8.0 and some other software based on our previous reports <sup>1-3</sup>. An analytical electron microscopic technique with an Energy-Dispersive X-ray spectroscopy analysis (EDXMA or EDX, Oxford Instruments. Model: INCA x-act.), and elemental mapping were employed for elemental analysis. The investigation of valence states of the fabricated electrodes was performed using X-ray photoelectron spectroscopy (XPS) by VG-Microtech Multilab 3000 spectrometer through a monochromatic Al-K $\alpha$  X-ray source.

The porosity and specific surface area of prepared MOFs were evaluated through the porosimetry analysis (BJH and BET analysis) by adsorption/desorption isotherms of nitrogen (N<sub>2</sub>) on a Beslorp apparatus (BELMAX, Japan). Before BET examination, the degassing process was performed for 24 h at 120 °C. The electrochemical studies were conducted through an Autolab/PGSTAT101 potentiostat/galvanostat (The Netherlands, Eco Chemie) instrument with a typical three-electrode and two electrode setups. Potentiostat/galvanostat equipment (Zahner/Zennium, Zahner, Germany) was used for EIS investigations. Then, data fitting with an equivalent electrical circuit were proposed through the Z-view software.

#### **S1.4 Electrochemical investigations**

For analysing the electrochemical performance of the bi-MMOF modified electrodes as a supercapacitor, electrochemical impedance spectroscopy (EIS), cyclic voltammetry (CV), and galvanostatic charge/discharge (GCD) techniques were examined in three-electrode and two-electrode setups as following.

##### ***S1.4.1 Electrochemical studies in a three-electrode setup***

The saturated calomel electrode (SCE) as a reference electrode and the stainless steel plate as a counter electrode were used. Also, various MOF/Ni-Foam (MOF/NF) electrodes were employed as working electrodes. All of the measurements were performed in the aqueous solution (3.0 M KOH) at room temperature. CV measurements in a three-electrode setup were carried out on the various potential windows vs. SCE at 10 to 50 mV s<sup>-1</sup> scan rates. GCD experiments were conducted in a variety of current densities from 2.5-20 A g<sup>-1</sup>. The EIS data were recorded at OCP (open circuit potential) over 100 KHz to 10 mHz frequency range at 10 mV AC.

##### ***S1.4.2 Electrochemical studies in a two-electrode setup***

The aqueous symmetric supercapacitors (SSCs) were fabricated from a cellulose separator and two similar bi-MMOF/Ni-Foam electrodes with 3.0 M KOH aqueous electrolyte. The assembled symmetric supercapacitor was employed for the electrochemical examination in a two-electrode cell. The electrochemical studies were conducted thoroughly at a similar condition as the three-electrode system (**Scheme 1**).

### S1.4.3 Evaluation of the electrochemical parameters

The specific capacitance ( $C_s$ ) of the MOF modified electrodes obtained through the CVs curves via **Equation S1**:<sup>4</sup>

$$C_s = \int I dV / m v \Delta V \quad (\text{F g}^{-1}) \quad (\text{Eq. S1})$$

Where the integration of the cathodic range of CVs is  $\int I dV$ , while the range of the potential and the scan rate are  $\Delta V$  and  $v$  ( $\text{V s}^{-1}$ ), respectively. The active material mass of the MOF electrode is  $m$  (g). Also, the  $C_s$  for the single electrodes may be evaluated through the discharge curves using **Equation S2**:<sup>5</sup>

$$C_s = I \Delta t / m \Delta V \quad (\text{F g}^{-1}) \quad (\text{Eq. S2})$$

Where the discharge current is  $I$  (A), the range of discharge time is  $\Delta t$  (s),  $\Delta V$  (V) is the range of the discharge potential except for the IR drop. However,  $C_s$  ( $\text{F g}^{-1}$ ) and  $m$  (g) are the same as the explanations mentioned above. The active material mass loaded on the MMOF electrode was around 1.0 mg. It must be noted for calculating the  $C_s$  value of the SSCs device, the active material's total mass of the negative and positive electrodes is  $m$  (g). For the electrode materials with battery-like behavior, the specific capacity ( $\text{mA h g}^{-1}$ ) is calculated using using **Equation S3**:

<sup>4</sup>

$$\text{Specific Capacity} = \frac{C_s \Delta V}{3.6} \quad (\text{mA h g}^{-1}) \quad (\text{Eq. S3})$$

The energy density ( $E_s$ ) and the power density ( $P_s$ ), derived from the GCD curves of symmetric supercapacitors, were estimated based on **Equations S4** and **S5**:<sup>4</sup>

$$E_s = C_s \Delta V^2 / 2 \times 3.6 \quad (\text{Wh kg}^{-1}) \quad (\text{Eq. S4})$$

$$P_s = (E_s \times 3600) / \Delta t \quad (\text{W kg}^{-1}) \quad (\text{Eq. S5})$$

Where the  $C_s$ ,  $\Delta V$ , and  $\Delta t$  are similar to the symbols in **Equation S2**.

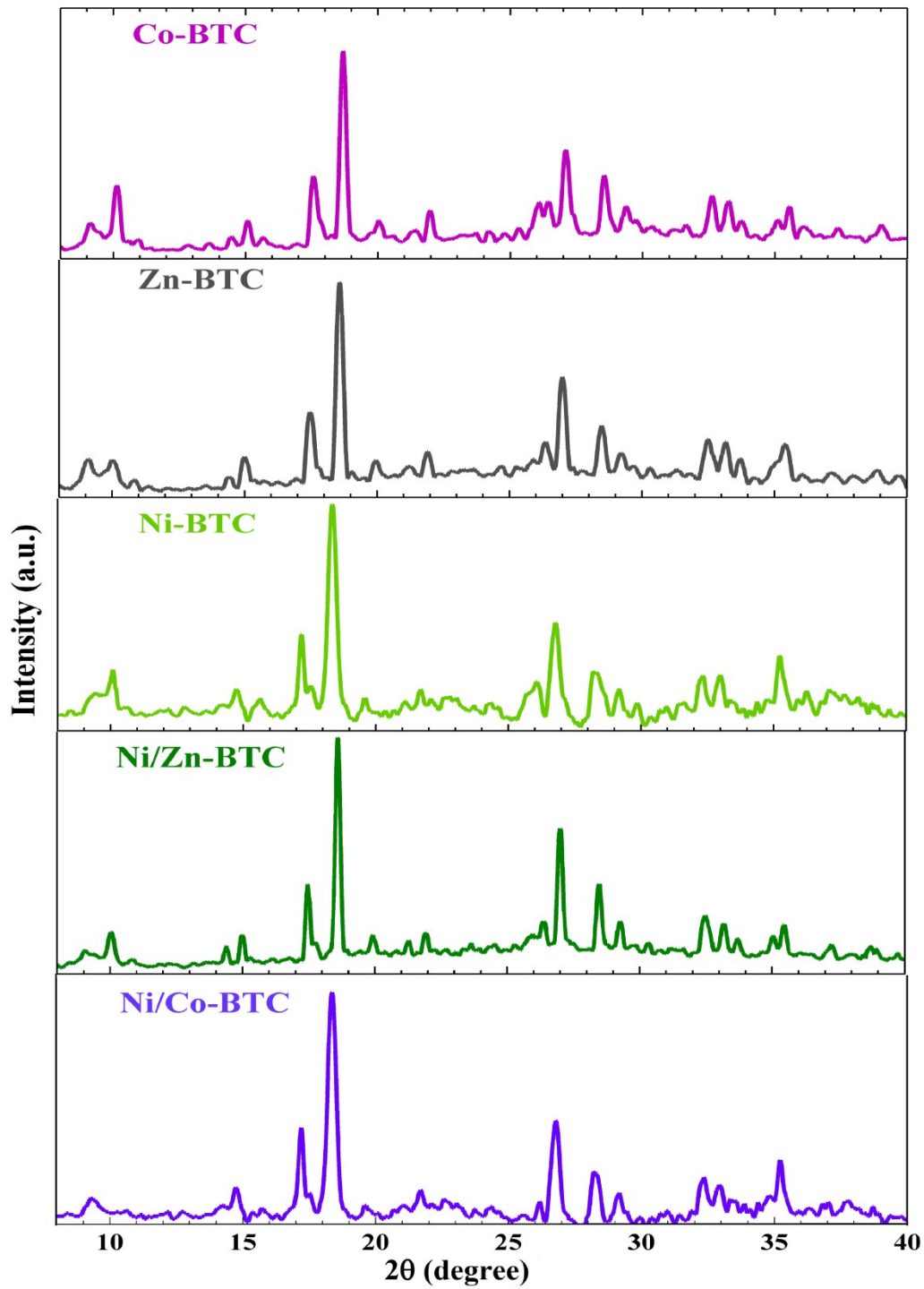


**Figure S1.** X-ray diffraction patterns of the synthesized MOFs electrodes.

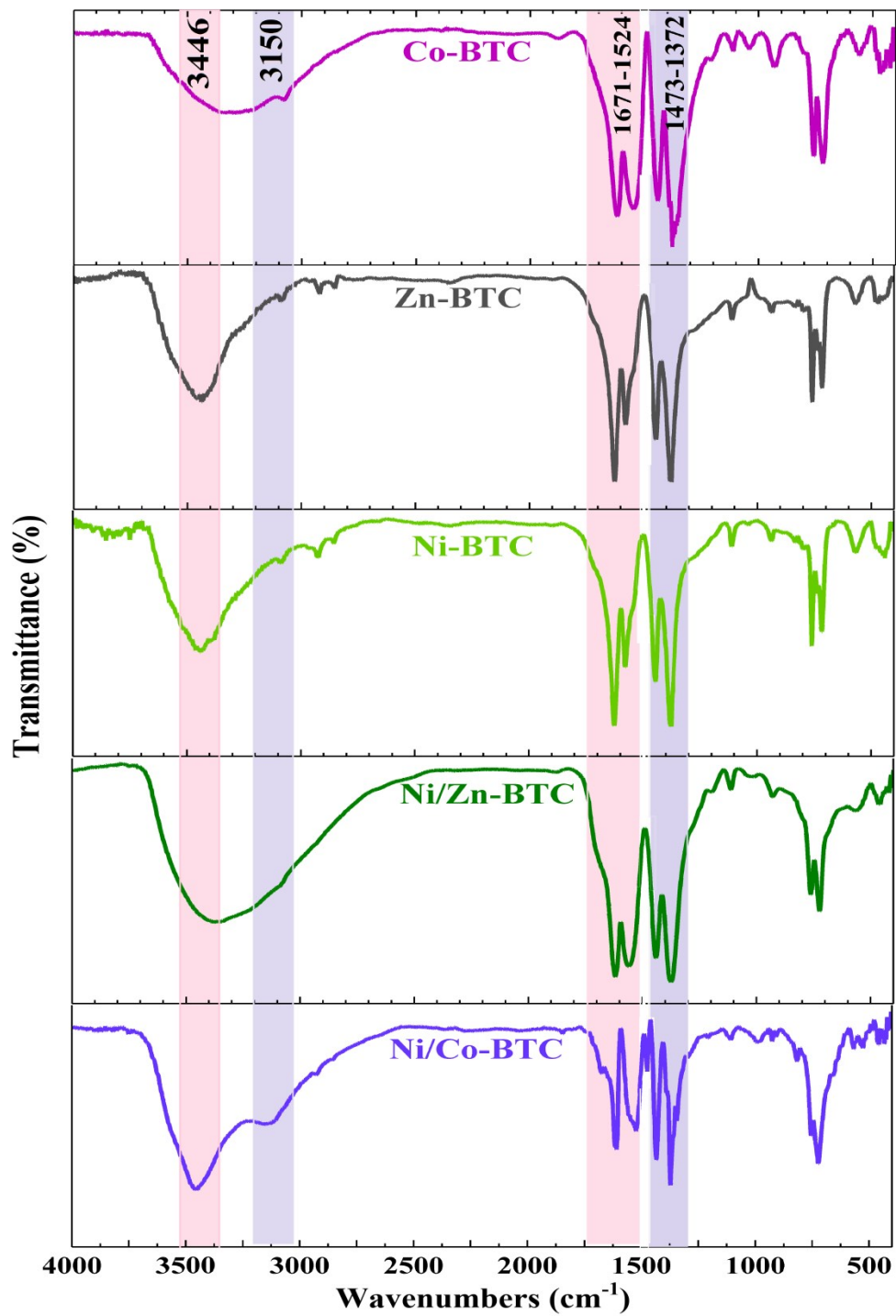
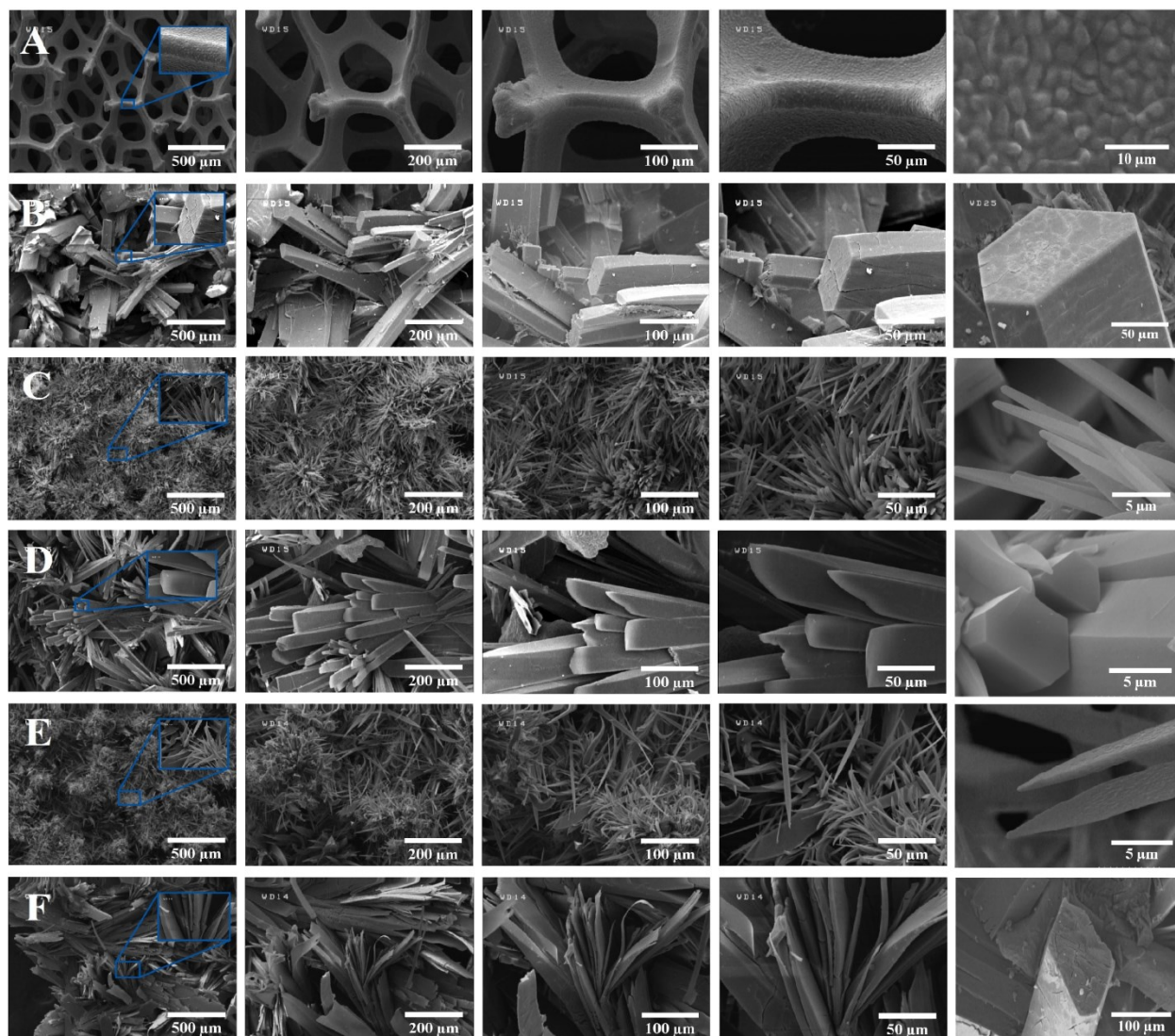
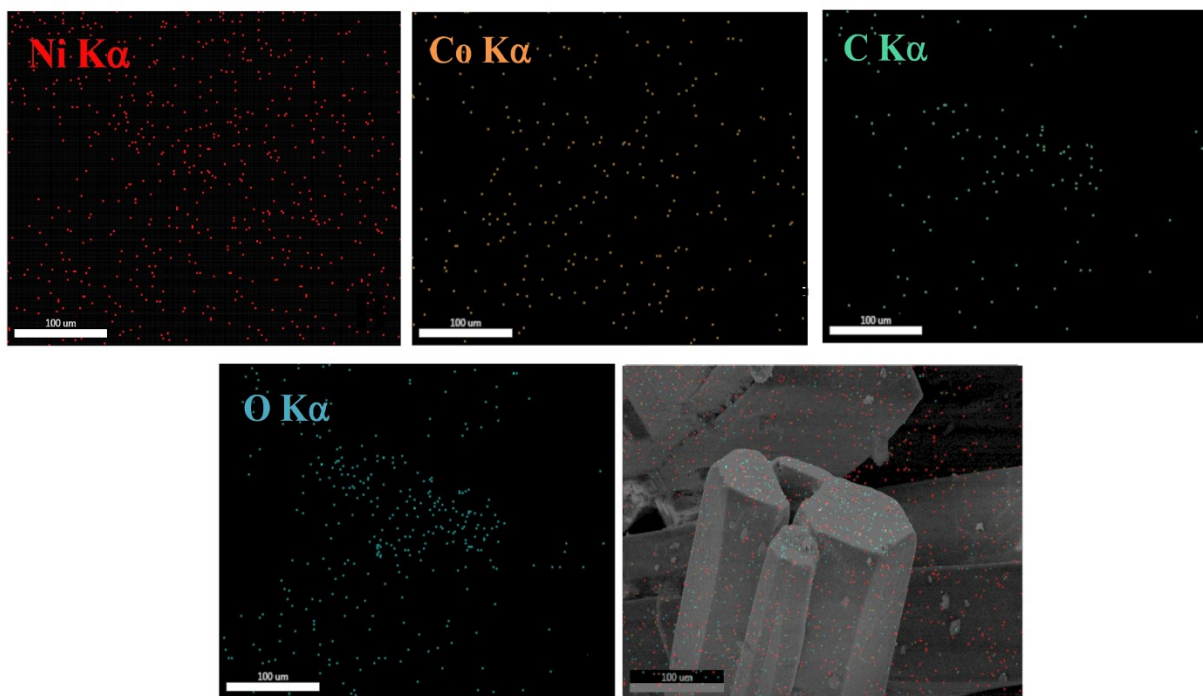
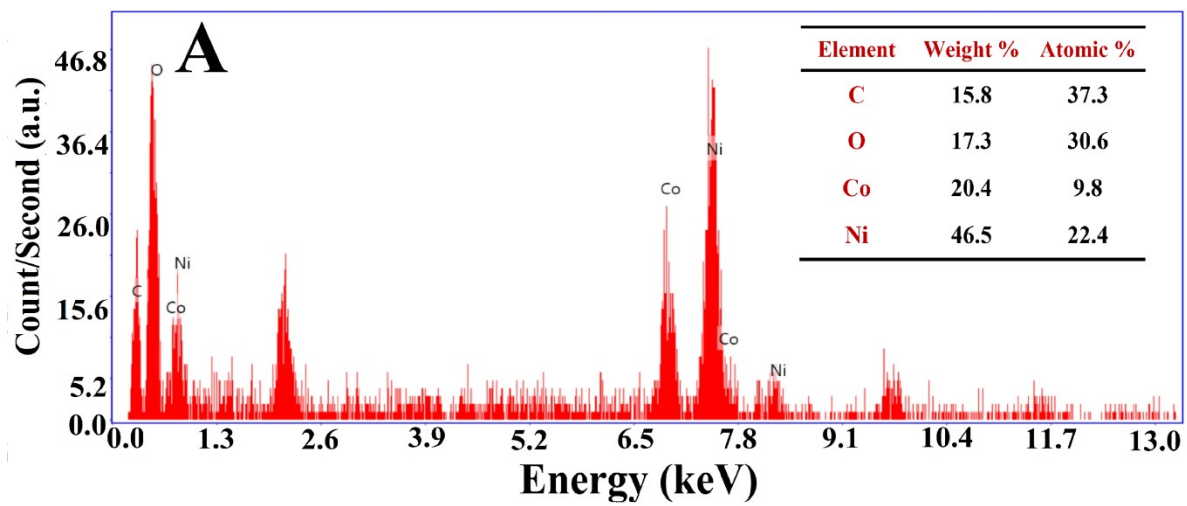
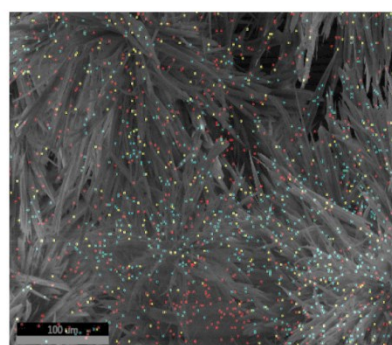
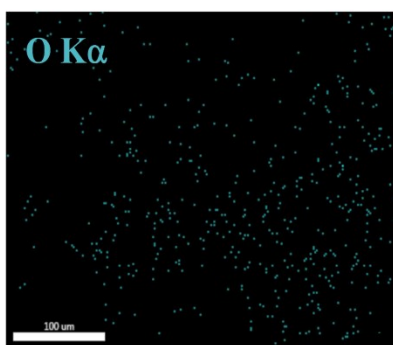
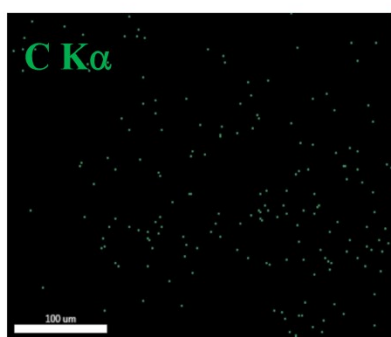
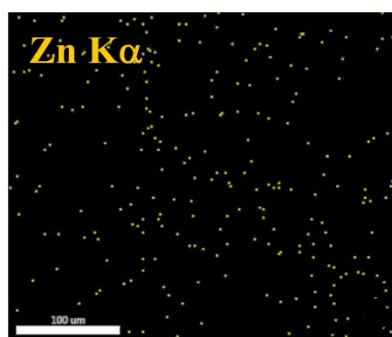
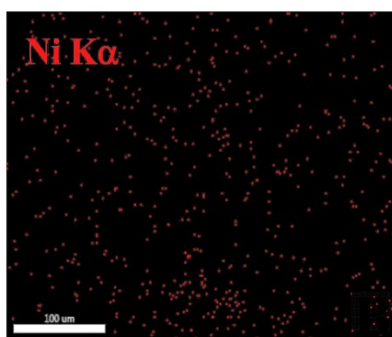
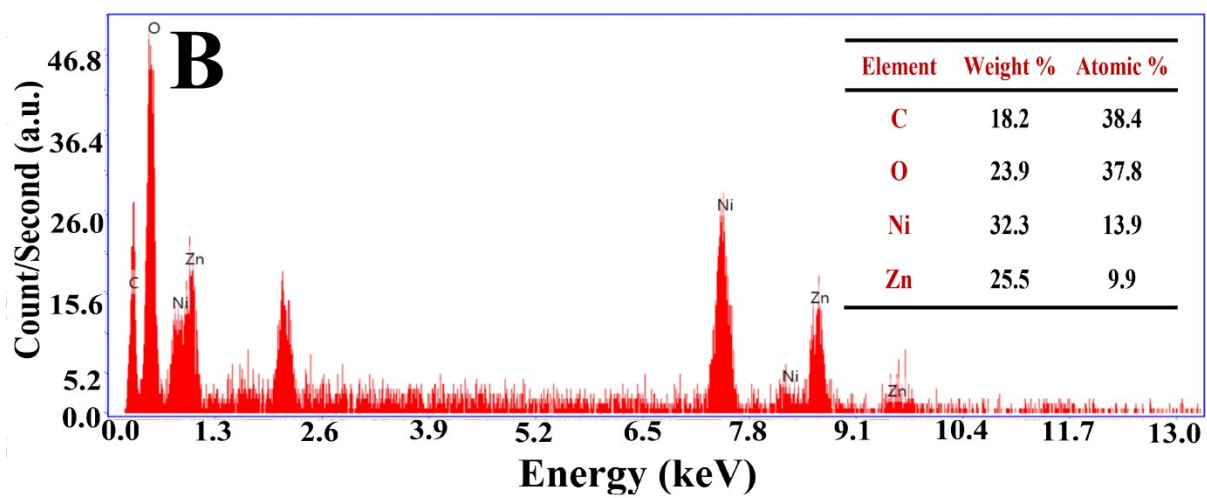


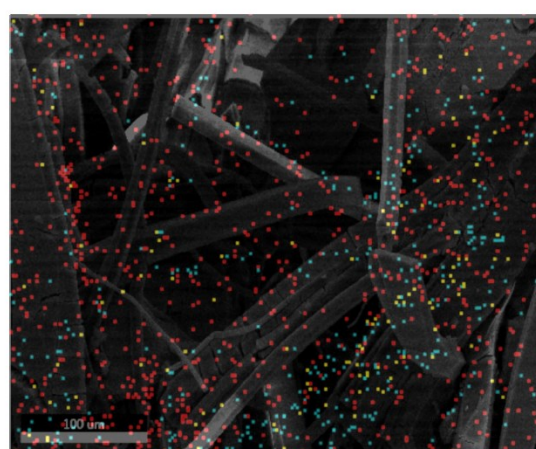
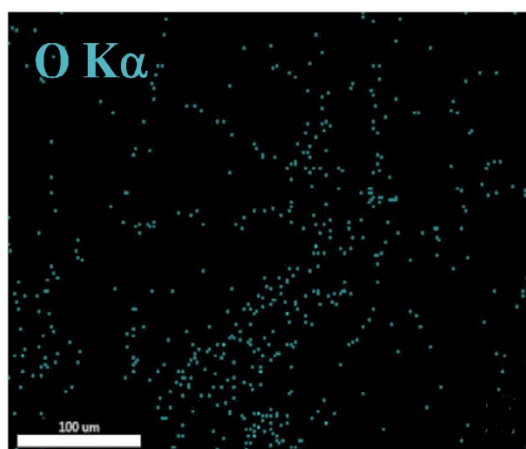
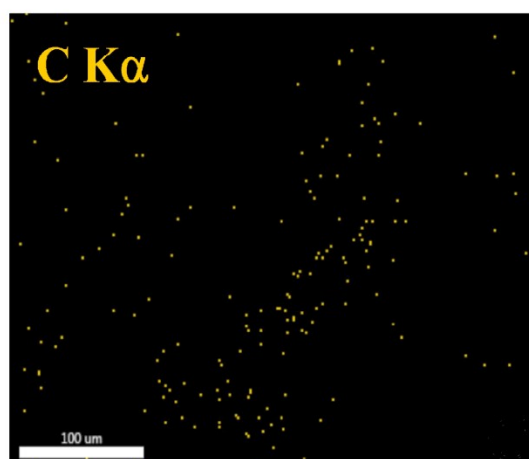
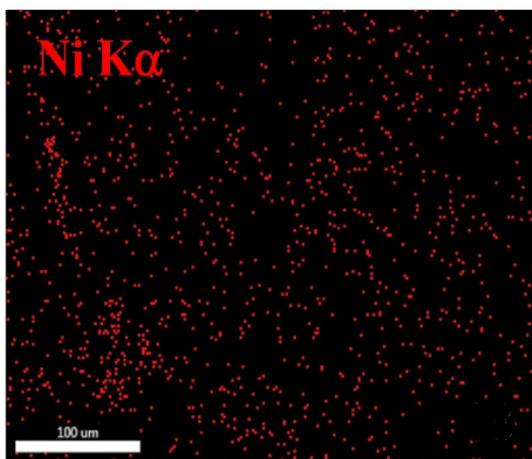
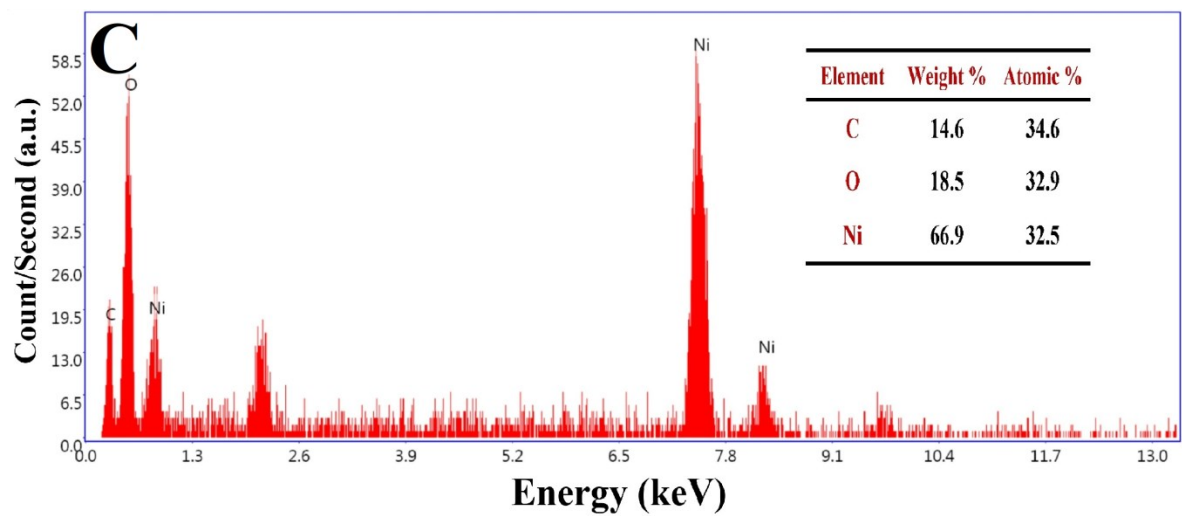
Figure S2. FT-IR spectrum recorded for the synthesized MOFs.

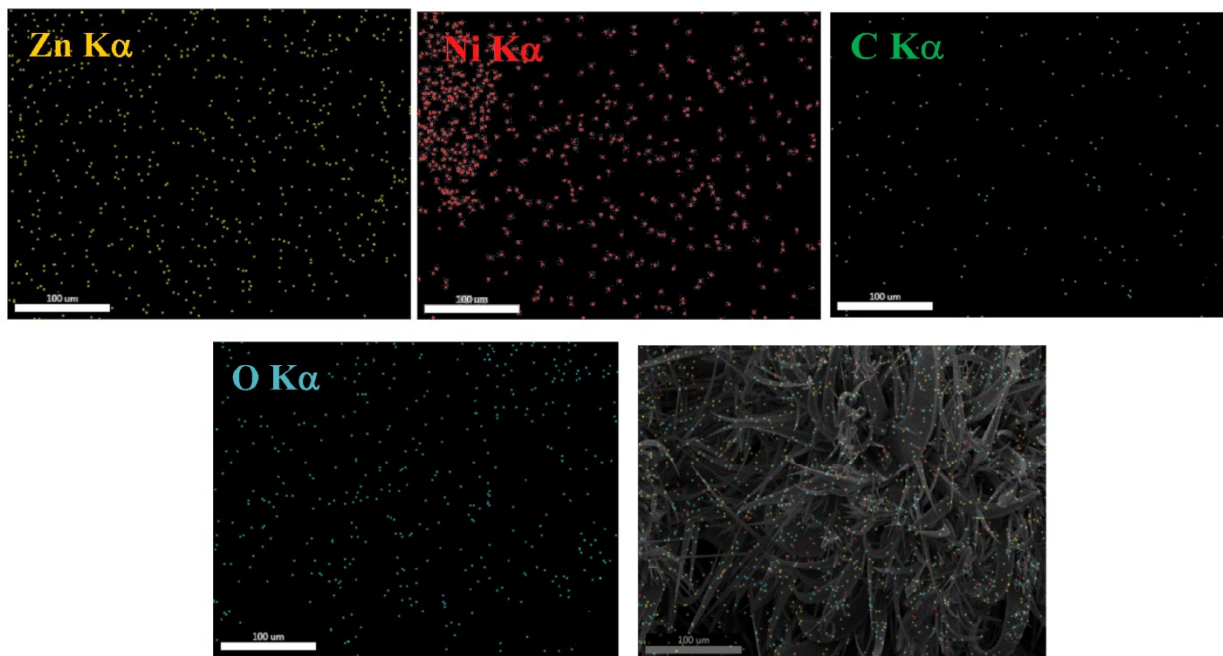
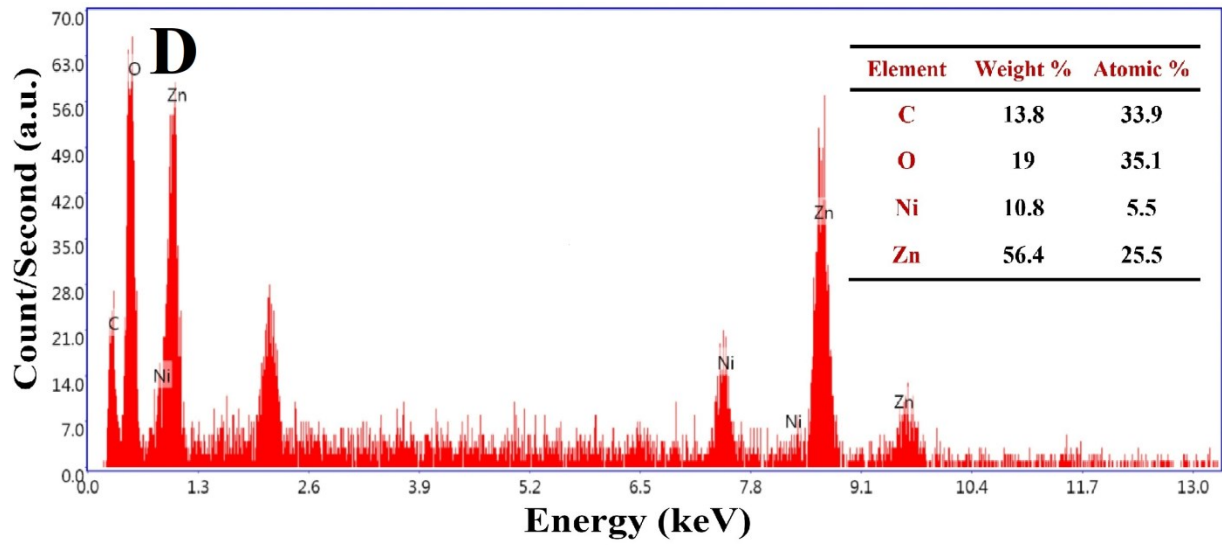


**Figure S3.** FE-SEM images of the Ni-foam substrate and the MMOF modified electrodes in different magnifications: (A) Ni-foam substrate, (B) Ni/Co-BTC, (C) Ni/Zn-BTC, (D) Ni-BTC, (E) Zn-BTC, and (F) Co-BTC electrodes.









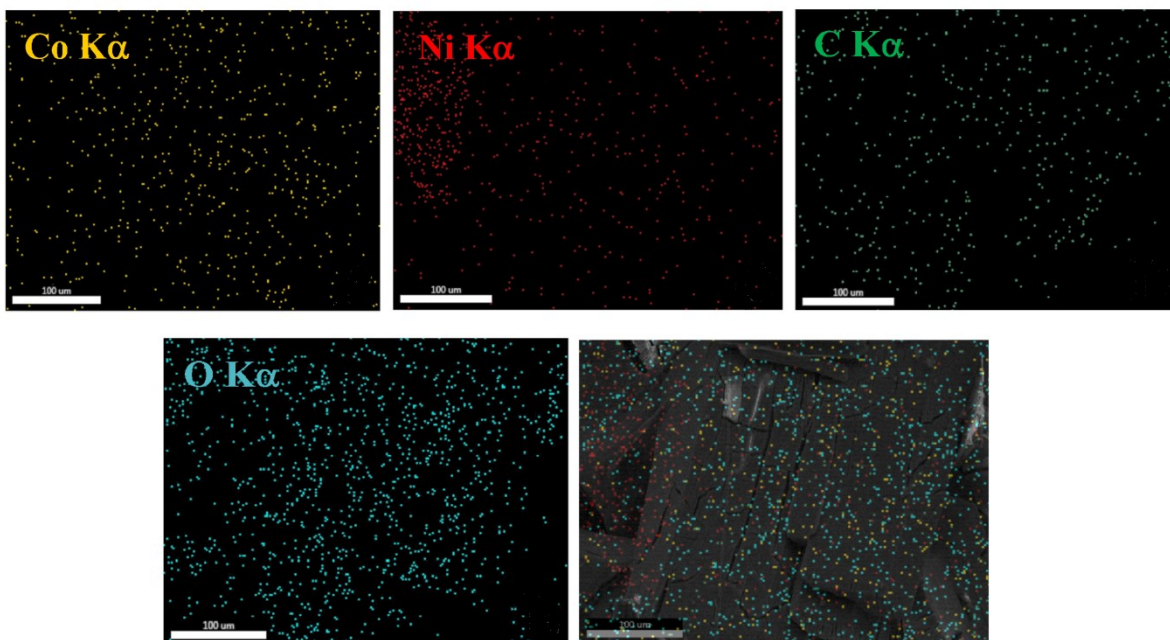
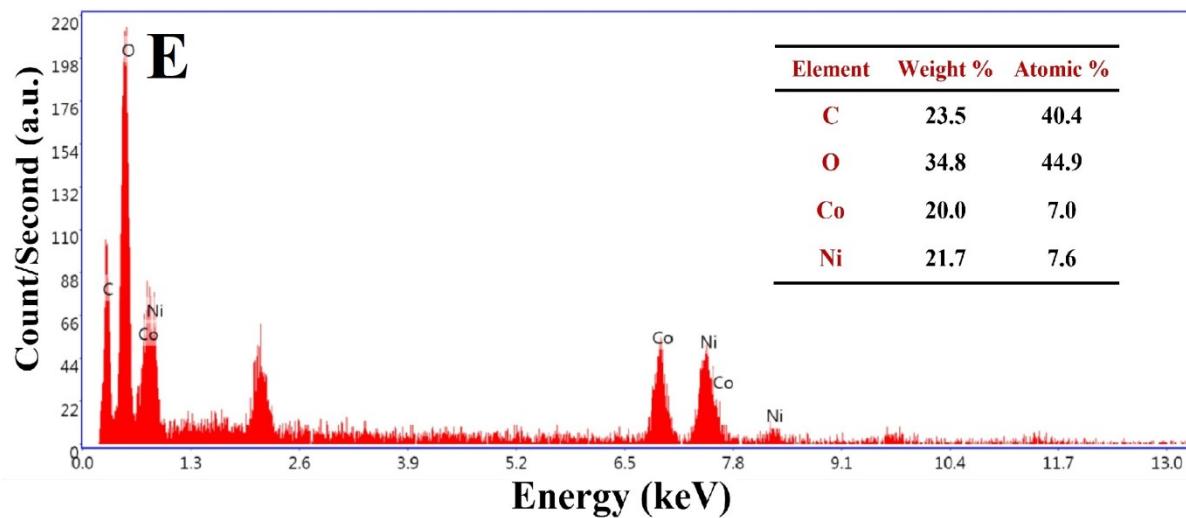


**Figure S4.** EDX spectrum of (A) Ni/Co-BTC, (B) Ni/Zn-BTC, (C) Ni-BTC, (D) Zn-BTC, (E) Co-BTC electrodes, elemental mapping of all the elements present in the electrodes, and overall elemental mapping images of these compounds.

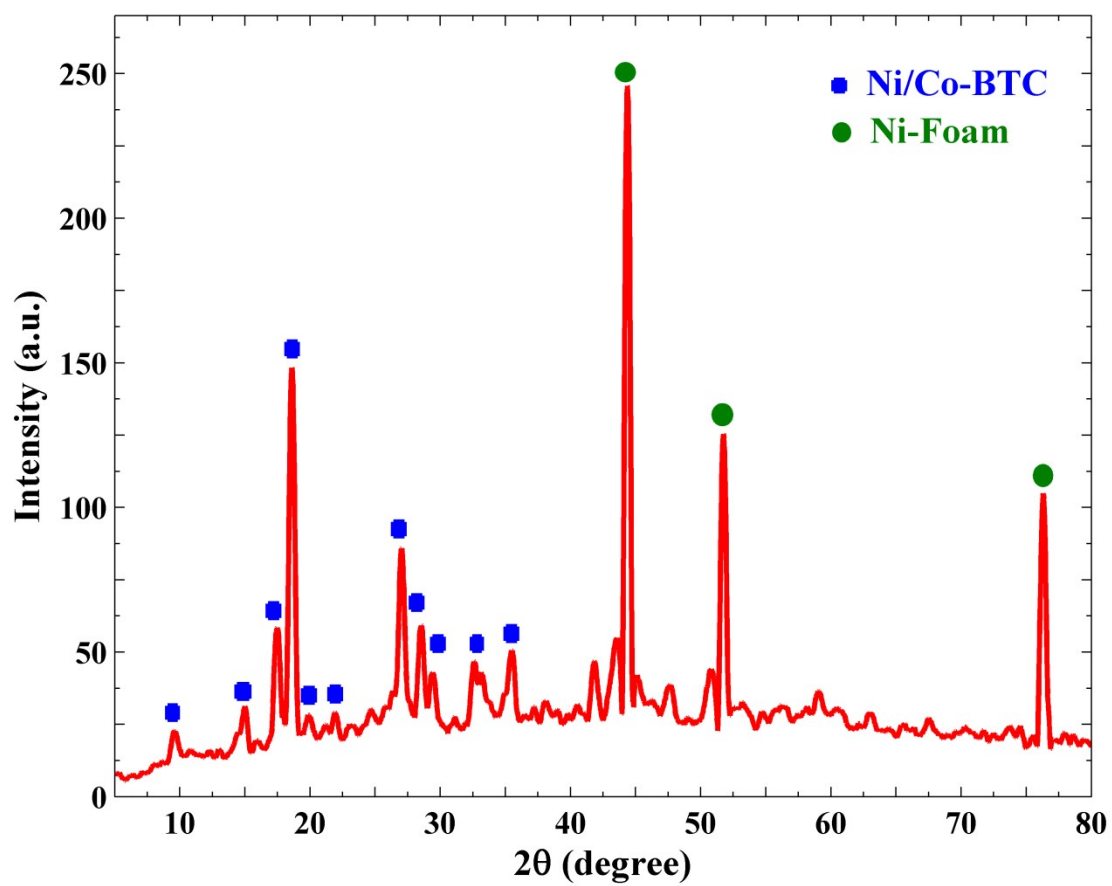


**Figure S5.** XRD pattern of MOF//Ni-foam electrode and the representation of Ni/Co-BTC and Ni-foam corresponding peaks.

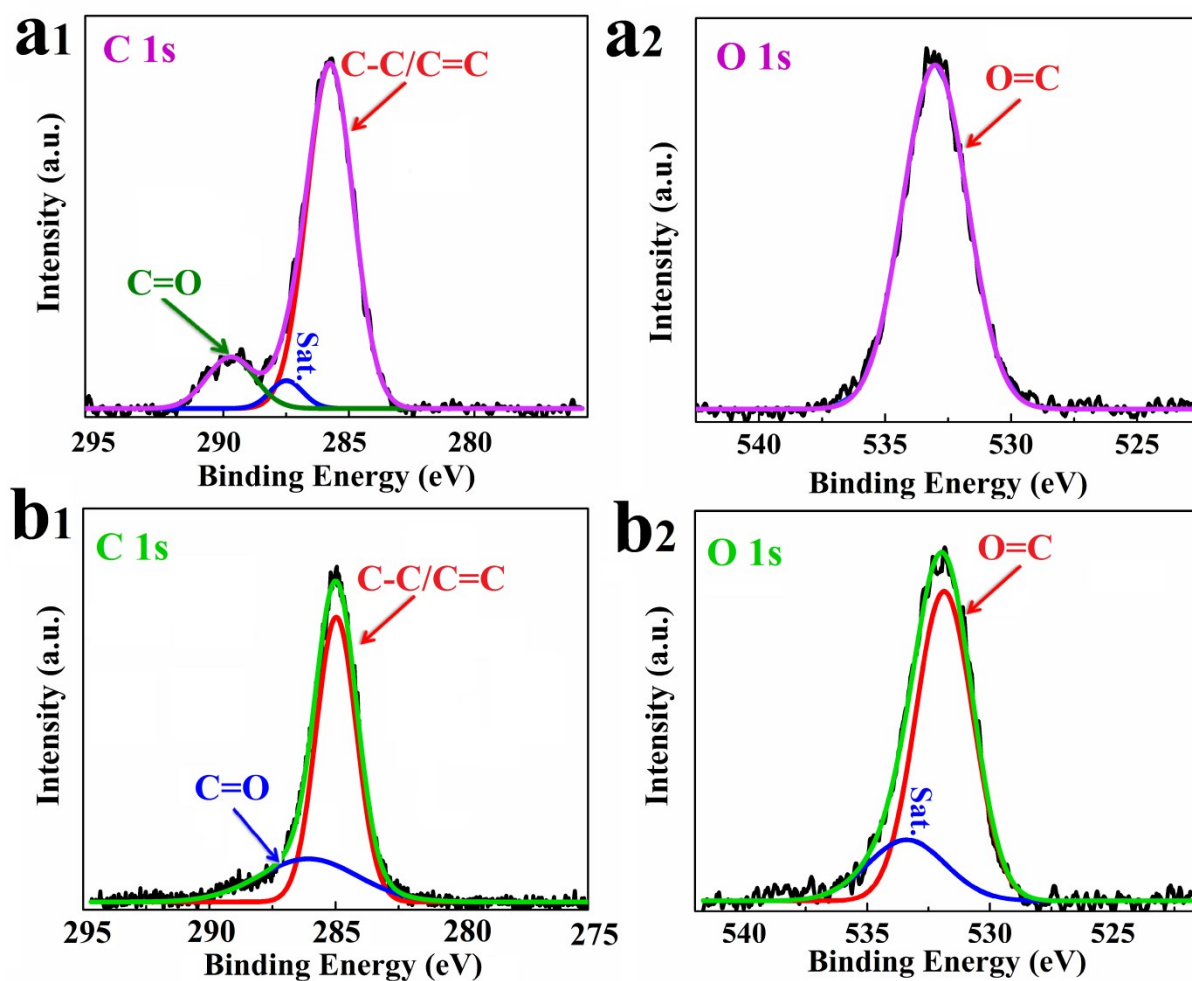


**Figure S6.** XPS high-resolution spectra: (a<sub>1</sub>, and b<sub>1</sub>) C 1s, and (a<sub>2</sub>, and b<sub>2</sub>) O 1s for (a) Co/Ni-BTC and (b) Ni/Zn-BTC MOF electrodes.

## Note S2: Statistical and stereometric analyses

The functional parameters of the stratified surfaces originate from the bearing area curve (BAC) or Abbott-Firestone curves. These curves (**Figure S7a<sub>1</sub>-S7e<sub>1</sub>**) are a description of the texture of the sample surfaces. The BAC is defined as the ratio of length obtained by intersecting a line at different heights to the profile. The BAC could be one of the most significant methods in surface profilometry characterization for the assessment of electrolyte accessibility on the surface of the electrodes and the evaluation of ions diffusion and migration length in the electrode/electrolyte interface. The core roughness depth ( $S_k$ ) is the depth of the core roughness while eliminating of the predominant valleys and peaks has occurred.  $S_k$  can be used similar to  $S_z$  for the nominal roughness if anomalous valleys or peaks influence on the measurement adversely. Above the core roughness, the measure of the peak height is  $S_{pk}$ , and under the core roughness the measure of the valley depth is  $S_{vk}$ . The  $S_{pk}$  in larger quantities indicates a sample surface is composed of higher peaks so that the sample contact area became higher. Thus, higher  $S_{pk}$  and, in a similar attitude, higher  $S_{vk}$  are the advantages for better electrochemical performance.  $M_{r1}$  and  $M_{r2}$  comprise the structure related to the  $S_{pk}$  and  $S_{vk}$ , respectively, the accordance description about these parameters inserted in the **Note S2.1**, briefly. According to the results in **Figure S7a<sub>1</sub>-S7e<sub>1</sub>** and **Table S1**, Ni/Co-BTC electrode with  $S_k=5.074$ ,  $S_{pk}=2.207$ , and  $S_{vk}= 2.201$ , and Ni-BTC electrode with  $S_k= 6.113$ ,  $S_{pk}= 2.661$ , and  $S_{vk}= 2.603$  provide higher space and contact area in the electrode/electrolyte interfaces. In comparison, the Co/BTC electrode with  $S_k= 1.644$ ,  $S_{pk}= 0.3862$ , and  $S_{vk}= 0.4890$  has the minimum space and contact area, so supplied the poor electrochemical performance in comparison to other electrodes.  $M_{r1}$  (upper bearing area) and  $M_{r2}$  (lower bearing area) have similar approaches. Also, Ni/Zn-BTC electrode with having the highest  $M_{r2}$  and significant  $M_{r1}$  can be a good candidate for this field of application.

For more investigation the texture of the MOFs electrodes, particle analyses carried out via employing the watershed algorithm.<sup>6</sup> This method could provide a unique visualization of the motifs, including the hills of the surfaces. The outcomes of this study were revealed in **Figure S7a<sub>2</sub>-S7e<sub>2</sub>**, and **Table S2** and the related parameter were specified in **Note S2.2**. The watershed segmentation processing divides an image into unique regions (of the peaks and valleys). So, the 3-D surface of the analyzed electrodes is divided into motifs of significant shapes. The number of motifs demonstrates the number of segmented peaks. Besides, some important parameters are introduced via this analysis, such as mean height, mean area, and mean volume of the peaks.

From the other point of view, the watershed segmentation study allowed us to identify important differences in the surface structure of the MMOF electrodes, arising from the participation of different ions in the composition of the electrode materials. For example, a specimen with a larger number of motifs with higher heights provides a superior contact surface area for ion accessibility on the electrode/electrolyte interface and accelerates the kinetics of ion diffusions.

According to the collected data of the particle analysis Ni/Co-BTC, Ni/Zn-BTC, and Ni-BTC electrodes have significant features compared to Zn-BTC and Co-BTC electrodes. In agreement with the previous outcomes, the results derived from surfaces' segmentation indicated that the highest number of motifs, density, mean height, and mean number of the neighbors were related to Ni/Co-BTC and Ni/Zn-BTC electrodes. At the same time, the other parameters such as the mean pitch and mean of equivalent diameters were remarkable, too. Significantly Ni/Co-BTC electrode, in comparison to the Ni/Zn-BTC electrode, has higher mean coflatness, mean compactness, mean roundness, and nearly vertical orientation. Thus, this electrode can be a better candidate for electrochemical applications.

Another stereometric analysis is the determination of the surface furrows. **Figure 7Sa<sub>3</sub>-7Se<sub>3</sub>** and **Table S3** indicate the furrow parameters' quantities, including the maximum depth, mean depth, and mean density of MOF modified electrodes calculated from AFM images with  $1\mu\text{m} \times 1\mu\text{m}$  scanning square areas. The behavior of the furrows is strongly dependent on the frequency range so that in the lower frequency range (e.g. 100 Hz) the furrows more or less behave like a perfect capacitor, while in the higher frequency range (e.g. 10 KHz) they behave like an ideal pore. Somehow, in wider and deeper furrows the effect will be even more pronounced. It could be concluded that the depth and density of furrows, as well as height quantities parameters simultaneously, could influence the electrochemical performance of the electrodes. So that, increasing these quantities leads to increasing the surface roughness.<sup>7</sup> According to the obtained furrow parameter results, the highest maximum depth of furrows was dedicated to the Ni/Co-BTC electrode (10.72 nm). In comparison the lowest quantity was observed in the Co-BTC electrode (1.67 nm). Moreover, the deepest mean depth of furrows was related to the Ni-BTC electrode (3.531 nm), and the shallowest one was found for the Co-BTC electrode (0.51 nm). Interestingly, the mean density of furrows in Co-BTC electrode (393328 cm/cm<sup>2</sup>) was the highest value and even more than Ni/Co-BTC electrode (308381 cm/cm<sup>2</sup>).

### S 2.1. The definition of statistical and stereometric parameters

According to ISO 25178-2:2012 <sup>8</sup> for 3D surface roughness, the statistical parameters are described as follows:

**(a)** *The height quantities distribution parameters* are a class of the surface parameters specifies surface finish parameters respect to the Z-axis perpendicular to the surface.

(Sa): Arithmetical mean height is the mean value of the surface roughness.

(Sq): Root mean square height or RMS value of the height irregularities is the standard deviation of the height distribution and is calculated from the variance of data.

(Sp): Maximum peak height is the height between the highest peak and the mean plane.

(S<sub>v</sub>): Maximum pit height is the depth between the mean plane and the deepest valley.

(Sz): Maximum height is the height between the highest peak and the deepest valley.

(Sa): Arithmetical mean height is the mean surface roughness.

**(b)** *The functional parameters* are ascribed as the distribution of heights and calculated from the Abbott-Firestone curve obtained by the integration of the height distribution on the whole surface. One of their aims is characterizing the functional behaviour of the surface contact.

(Smr (c) or M<sub>rc</sub>): Areal material ratio is the bearing area ratio at a given height. Ratio of the area of the material at a specified height c (cut level) to the evaluation area. The Smr (c) is expressed as a percentage. For the Smr parameter, the height c is counted by default from the mean plane.

(S<sub>k</sub>): Kernel roughness depth or core height is the distance between the highest and lowest level of the core surface.

(S<sub>pk</sub>): Reduced peak height is the thickness of BAC above the core surface.

(S<sub>vk</sub>): Reduced valley depth is the bearing curve thickness below the core surface.

**(c)** *Spatial parameters* describe topographic characteristics based upon spectral analysis. They quantify the lateral information present on the X- and Y-axes of the surface.

(Str): Texture-aspect ratio is the ratio of the shortest decrease length in 0.2 from the autocorrelation, on the greatest length. This parameter has a result between 0 and 1. For the isotropic surface in all directions with the same characteristics, the value of S<sub>tr</sub> is near 1. For the anisotropic surface with an oriented structure and/or periodical structure, the value of S<sub>tr</sub> is near 0.

## S2.2 The definition of the surface segmentation parameters

The parameter of the motif analysis for the 3-D surface roughness are described according to ISO 25178-2: 2012 as follows <sup>1, 8</sup>:

- (a) Number of motifs: Average value of number of all motifs.
- (b) Mean height [nm]: Average value of height between highest saddle point and peak.
- (c) Mean area [ $\mu\text{m}^2$ ]: Average value of horizontal area enclosed inside the course line.
- (d) Mean perimeter [ $\mu\text{m}$ ]: Average value of the length of the perimeter of the grain.
- (e) Mean of equivalent diameters [ $\mu\text{m}$ ]: Average value of the diameter of the disk whose area is equal to the area of the grain.
- (f) Mean of mean diameters [ $\mu\text{m}$ ]: Average value of mean diameters.
- (g) Mean of min / max diameters [ $\mu\text{m}$ ] / [ $\mu\text{m}$ ]: Average value of the smallest / biggest diameter of the grain measured from its center of gravity.
- (h) Mean of min / max diameter angles [ $^\circ$ ] / [ $^\circ$ ]: Average value of the angle of the smallest / biggest diameter of the grain measured from its center of gravity, in degrees, with  $0^\circ$  at the right side,  $-90^\circ$  at the top,  $90^\circ$  at the bottom.
- (i) Mean form factor: Average value of ratio between the area of the grain and the squared perimeter.
- (j) Mean aspect ratio: Average value of ratio between the maximum diameter and the minimum diameter. If the value is close to 1, the form of the grain is close to the form of a disk. If the value is high, the grain is oblong.
- (k) Mean roundness: Average value of the ratio between the area of the grain and the area of the disk having as diameter the maximum diameter of the grain. This value is close to 1 for a circular grain, and smaller than 0.5 for an oblong grain.
- (l) Mean compactness: Average value of ratio between the equivalent diameter and the maximum diameter. This ratio is close to 1 for a grain with the form of a disk, or smaller than 0.5 for an oblong grain.
- (m) Mean orientation [ $^\circ$ ]: Average value of angle between  $0^\circ$  and  $180^\circ$  of the biggest axis of the grain, measured in the trigonometric direction ( $0^\circ$  at the right side,  $180^\circ$  at the left side,  $90^\circ$  on top).

### **S2.3 The description of fractal dimension calculating method**

Morphological characterizations of mono-metallic and mix-metallic MOF electrodes were investigated via fractal dimensions Concept ( $D_f$ ). For this goal, Cube-counting or box-counting method was employed. Some related descriptions of this method are available here.

The definition of box-counting fractal dimension is the basis of the cube counting method and this method is illustrated in our previous work <sup>2</sup>. Based on the slope of the linear portion of a plot of  $\log N(\varepsilon)$  versus  $\log \varepsilon$ , fractal dimension  $D_f$  could be derived directly. In this method, the number of cubes  $N(\varepsilon)$  of size  $\varepsilon$  ( $\varepsilon \leq 1$ ), which cover the image, were estimated. Each of the cubes has pixels with nonvanishing height in it.  $N(\varepsilon)$  can be measured by  $N(\varepsilon) \propto \varepsilon^{-D_f}$ . By changing the size of the cube ( $\varepsilon$ ), a series of  $N(\varepsilon)$  and  $\varepsilon$  was produced. The simple fractal dimension  $D_f$  would derive from the slop of the  $\text{Ln } N(\varepsilon)$ - $\text{Ln } \varepsilon$  plot.

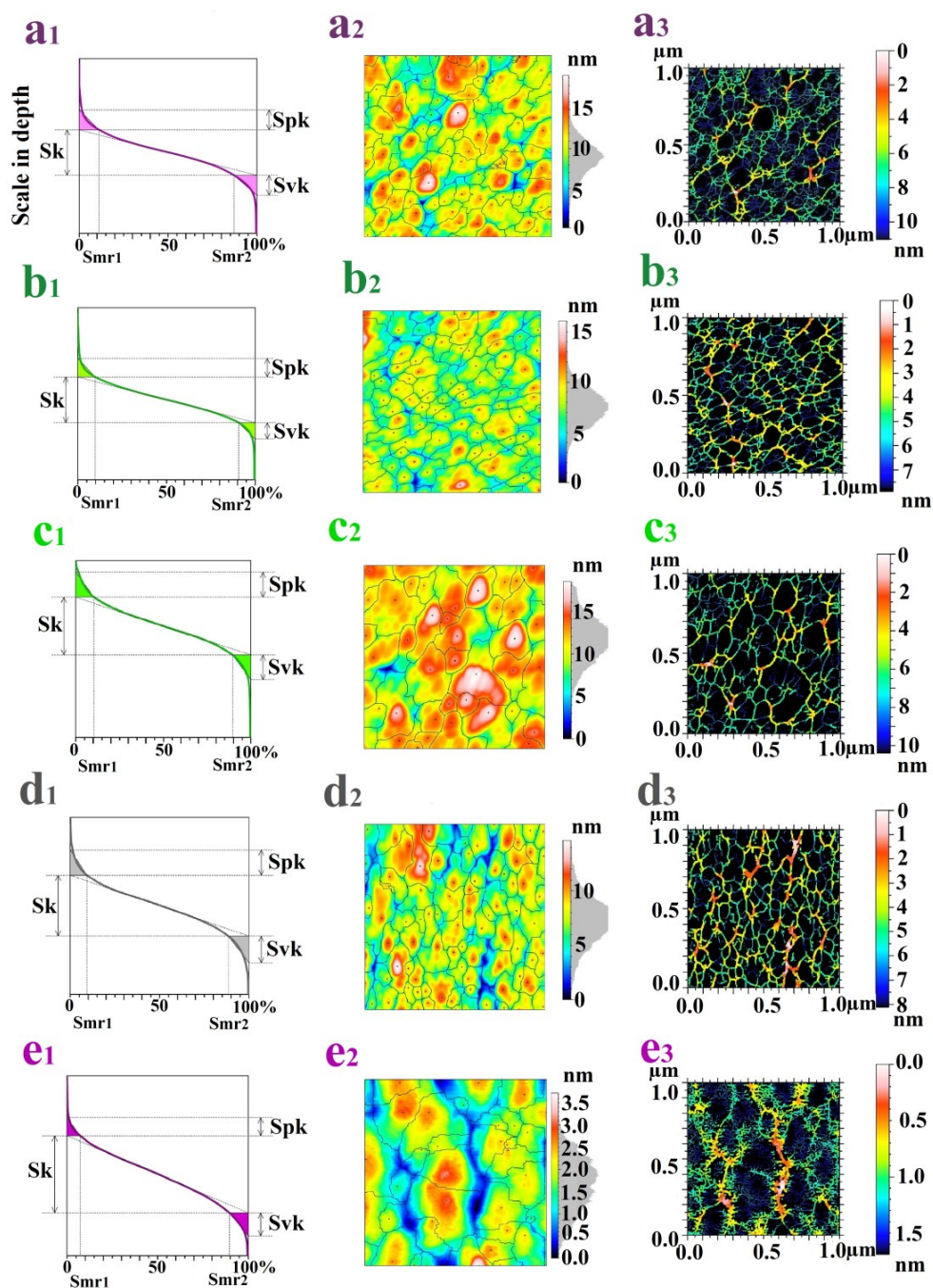


**Figure S7.** ( $a_1$ - $e_1$ ) represent the areal material ratio curves describing functional stratified surface parameters, ( $a_2$ - $e_2$ ) represent the motifs of significant shapes through the watershed segmentation algorithm, and ( $a_3$ - $e_3$ ) reveal the surface furrows of AFM images with  $1\mu\text{m}\times 1\mu\text{m}$  scanning square areas for the MOF electrodes: (a) Ni/Co-BTC, (b) Ni/Zn-BTC, (c) Ni-BTC, (d) Zn-BTC, and (e) Co-BTC.

**Table S1.** The basic features of the height quantities distribution and functional parameters (stratified surfaces) derived from the Bearing Area Curve (BAC) of the AFM images of m-MMOF and bi-MMOF, for scanning square areas of  $1\mu\text{m} \times 1\mu\text{m}$ .

Sample ID	The height quantities distribution					Functional stratified surface				
	Sa (nm)	Sq (nm)	Sp (nm)	Sv (nm)	Sz (nm)	Sk (nm)	Spk (nm)	Svk (nm)	Mr1 (%)	Mr2 (%)
	Average roughness	RMS	Max. peak height	Max. pit height	Max. height	Kernel roughness depth	Reduced peak height	Reduced valley height	Upper bearing area	Lower bearing area
<b>Ni/Co-BTC</b>	1.669	2.136	10.43	8.891	19.32	5.074	2.207	2.201	11.09	87.06
<b>Ni/Zn-BTC</b>	1.357	1.717	8.831	7.692	16.52	4.381	1.791	1.565	9.624	90.59
<b>Ni-BTC</b>	1.955	2.487	6.930	11.80	18.73	6.113	2.661	2.603	10.37	89.52
<b>Zn-BTC</b>	1.623	2.059	7.435	7.328	14.76	5.004	2.106	2.229	9.229	88.84
<b>Co-BTC</b>	0.4853	0.591	2.124	1.706	3.830	1.644	0.3862	0.4890	7.092	89.59

**Table S2.** Parameter values of shapes resulting from surface segmentation using the watershed segmentation algorithm of analyzing samples.

Parameter	Sample				
	Ni/Co-BTC	Ni/Zn-BTC	Ni -BTC	Zn-BTC	Co-BTC
Number of motifs [-]	92	88	43	84	40
Density [Particles/mm <sup>2</sup> ]	91,640,976	87,656,586	42,832,195	83,672,195	39,843,903
Mean height [nm]	8.329954	7.267684	11.442769	6.902151	1.518369
Mean area [ $\mu\text{m}^2$ ]	0.01091	0.011408	0.023346	0.011951	0.025097
Mean volume [ $\text{nm}^3$ ]	21000.096	19072.876	52803.148	21578.551	12396.859
Mean perimeter [ $\mu\text{m}$ ]	0.44626	0.472543	0.665066	0.475201	0.731089
Mean Nb of neighbors [-]	5.13	5.20	4.74	5.02	4.75
Mean of equivalent diameters [ $\mu\text{m}$ ]	0.107391	0.115117	0.161762	0.115929	0.159582
Mean of minimum diameters [ $\mu\text{m}$ ]	0.074755	0.081056	0.112838	0.078857	0.106806
Mean of maximum diameters [ $\mu\text{m}$ ]	0.151584	0.166278	0.225912	0.166595	0.232383
Mean of minimum diameter angles [°]	-12.04	-26.31	-7.55	-6.60	-2.42
Mean form factor	0.600994	0.613211	0.615226	0.6157015	0.504954
Mean aspect ratio	2.284127	2.136752	2.127471	2.233157	2.680540
Mean pitch [ $\mu\text{m}$ ]	0.124504	0.134103	0.185950	0.136437	0.204125
Mean coflatness [nm]	3.876840	2.903908	3.626154	3.145187	1.140655
Mean solidity	0.869116	0.874048	0.875252	0.879466	0.845535
Mean roundness	0.522621	0.510594	0.533373	0.506812	0.488708
Mean compactness	0.715417	0.708374	0.723443	0.705860	0.687560
Mean orientation [°]	74.76	49.52	68.91	88.00	81.47

**Table S3.** The furrows parameters of mono-metallic and mix-metallic MOF, for scanning square areas of  $1\mu\text{m} \times 1\mu\text{m}$ .

<b>Parameters</b>	<b>Unit</b>	<b>Ni/Co-BTC</b>	<b>Ni/Zn-BTC</b>	<b>Ni -BTC</b>	<b>Zn-BTC</b>	<b>Co-BTC</b>
<b>Maximum depth of furrows</b>	nm	10.72	7.443	9.906	8.119	1.676
<b>Mean depth of furrows</b>	nm	3.188	2.717	3.531	3.364	0.5179
<b>Mean density of furrows</b>	cm/cm <sup>2</sup>	308,381	267,563	211,683	240,870	393,328

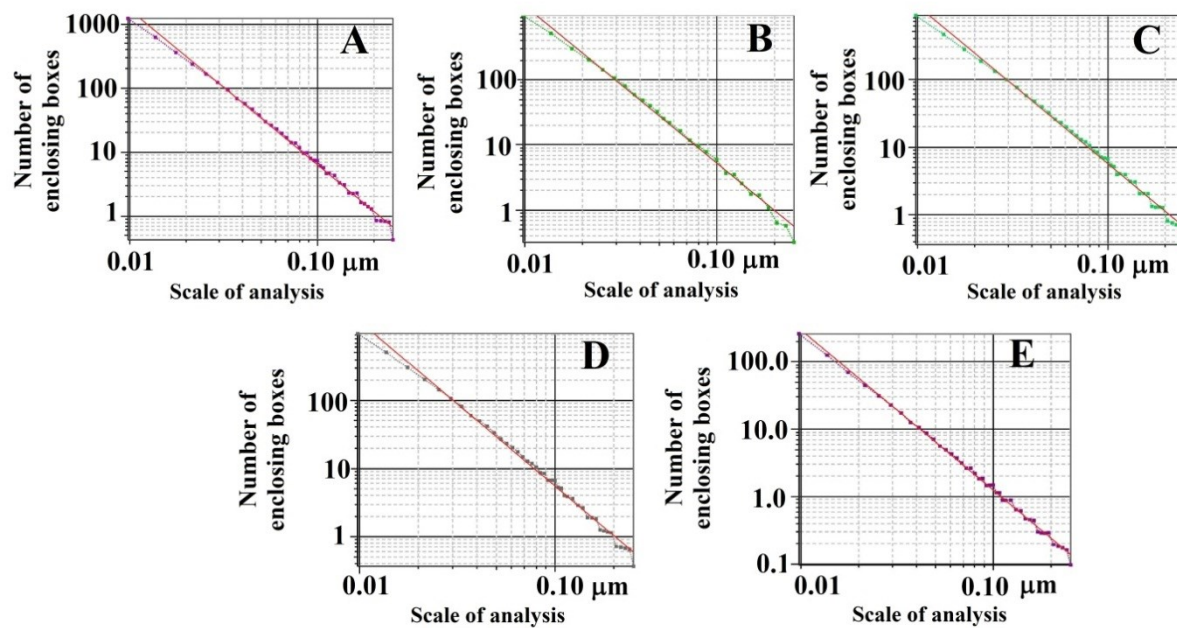


**Figure S8.** Logarithmic plot of number of enclosing boxes ( $N(\varepsilon)$ ) versus the scale of analysis ( $\varepsilon$ ) from the box-counting method for (A) Ni/Co-BTC, (B) Ni/Zn-BTC, (C) Ni-BTC, (D) Zn-BTC, and (E) Co-BTC.

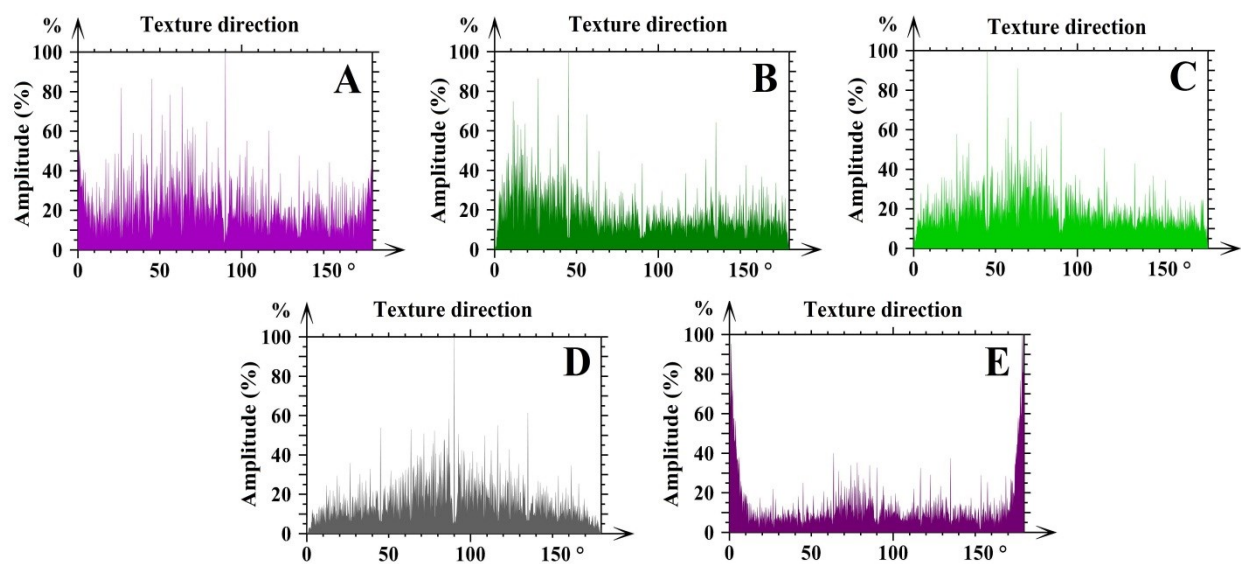


**Figure S9.** Cartesian representation of texture directions for the surfaces of the MOF electrodes: (A) Ni/Co-BTC, (B) Ni/Zn-BTC, (C) Ni-BTC, (D) Zn-BTC, and (E) Co-BTC.

**Table S4.** Fractal dimensions determined via the cube counting method and the texture aspect ratio ( $S_{tr}$ ) or isotropy and the texture direction of mono-fractal surfaces derived from AFM images of m-MMOF and bi-MMOF electrodes.

Sample ID	$D_f$	The texture direction of the surfaces			
		Isotropy (%)	1 <sup>st</sup> direction (°)	2 <sup>nd</sup> direction (°)	3 <sup>rd</sup> direction (°)
<b>Ni/Co-BTC</b>	2.419	53.19	90.02	45.01	63.52
<b>Ni/Zn-BTC</b>	2.460	65.27	44.99	26.45	11.27
<b>Ni-BTC</b>	2.326	66.12	45.00	63.51	90.00
<b>Zn-BTC</b>	2.415	28.17	90.00	135.0	116.5
<b>Co-BTC</b>	2.374	38.31	178.8	1.038	63.52

### Note S3. Quantitative description of the EIS measurements

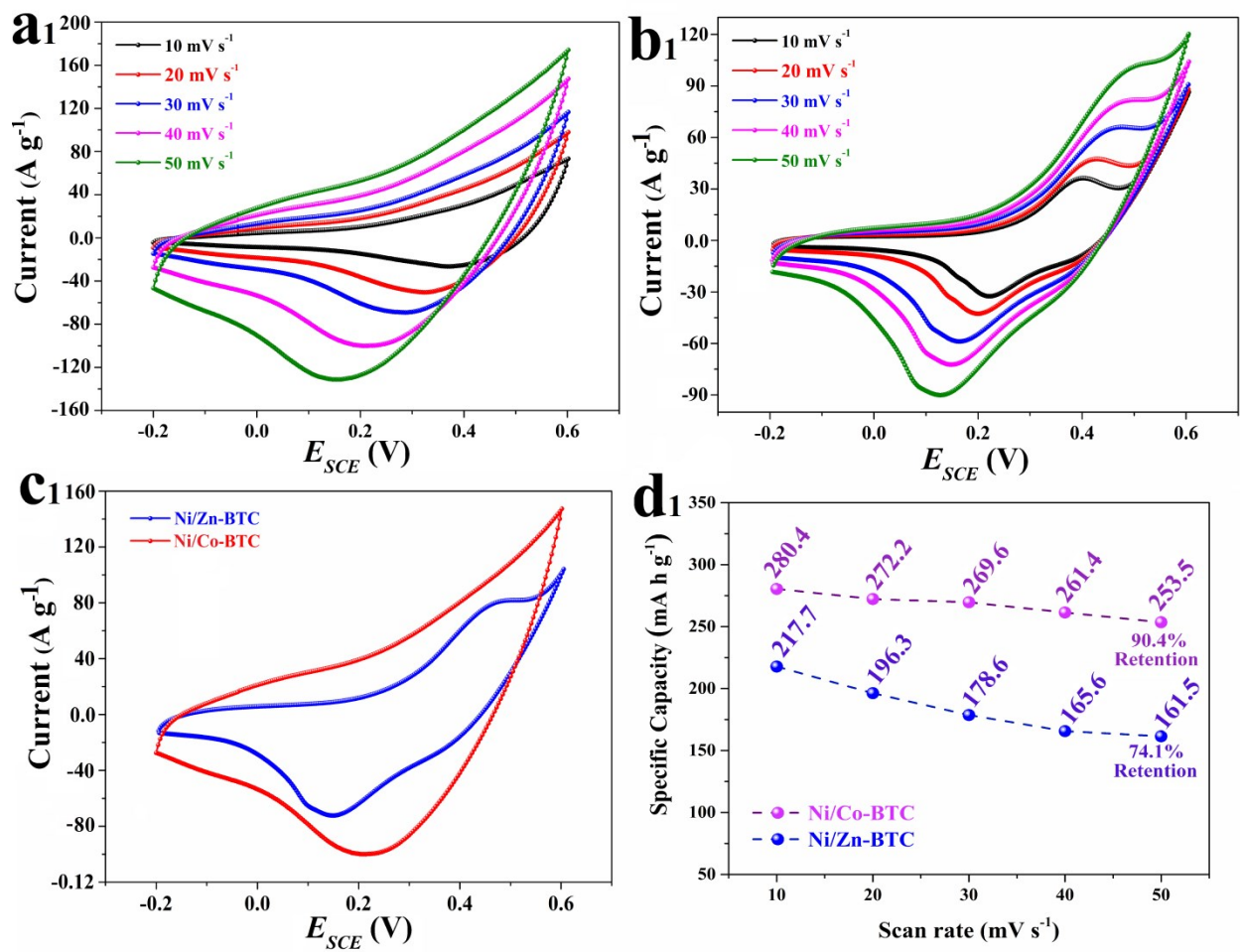
To provide an accurate quantitative description of the EIS, the proposed electrically equivalent circuits for the MOF electrodes were represented in the inset of **Figure 4A** and the relevant elements illustrated in **Table S5**. The inductive component,  $L$ , which appeared in the high-frequency regions, can be originated from the mutual inductance of the cables connecting the equipment<sup>9</sup> and the porous nature of the electrodes.<sup>10</sup> The  $R_s$ , the uncompensated resistance of the solution, is equal to  $1.11 \Omega$  for Ni/Co-BTC, which is approximately the average resistance of the parent m-MMOF with the dominant effect of the Co cations ( $R_s$ : Co-BTC=  $1.10 \Omega$  and Ni-BTC= $1.19 \Omega$ ). Also, this value is equal to the  $1.17 \Omega$  for Ni/Zn-BTC with the dominant effect of the Ni cations ( $R_s$ : Ni-BTC=  $1.19 \Omega$  and Zn-BTC= $1.12 \Omega$ ) (**Table S5**). The  $R_{ct}$ , the resistance of the charge transfer or ESR of the bi-MMOF modified electrodes is smaller than the parent m-MMOF modified electrodes. As expected, the lowest  $R_{ct}$  is related to the Ni/Co-BTC and Ni/Zn-BTC with  $0.063 \Omega$  and  $0.083 \Omega$ . In the case of Ni-BTC, the  $R_{ct}$  value is equal to  $0.085 \Omega$  indicate that the  $Ni^{2+}$  ion at Ni-BTC has significant electrochemical performances in comparison with  $Zn^{2+}$  and  $Co^{2+}$  ions at m-MMOF structures. A characteristic property of fractal surfaces is that they contain irregularities at many different length scales. Surface structure with self-similar roughness and fractal coverage influences the impedance (or admittance) spectra of electrode surfaces. In the case of a fractal carpet electrode, the modification appears only as a geometric pre-factor, in other words, these electrodes behave quasi-capacitively when the interfaces ideally polarizable. Therefore, if a capacitive electrode has fractal geometry, then the electrode impedance will be of the CPE form.<sup>11</sup>  $CPE_1$  is a presentation of the interfacial processes or the double-layer capacity. At the same time,  $CPE_2$  and  $W_s$  are the resistive and capacitive elements of the ionic transport/diffusion toward the electrode surfaces from the electrolyte. The frequency factor ( $n$ ) is a criterion for the standard of the electrode supercapacitive behavior. The frequency factor can be appeared in the following values: I)  $n < 0.5$ , II)  $0.5 < n < 1.0$ , and III)  $n=1.0$  refer to the lower, moderate and pure (ideal) supercapacitor behavior, respectively.

The quantities of the equivalent electrical circuit elements shown in **Table S5** confirm the obtained consequences in the previous sections and suggesting that the bi-MMOF electrodes have an excellent capacitive behavior in comparison to the m-MMOF electrodes.

**Table S5.** The values of elements for equivalent circuits (the inset of Fig. 4A) fitted to the Nyquist diagrams of Fig. 4A and the corresponding relative errors.

Sample ID	Element							
	L (H)	R <sub>s</sub> (Ω)	CPE <sub>1</sub> (Ω.s <sup>n</sup> )	n	R <sub>ct</sub> (Ω)	W <sub>s</sub> (Ω.s <sup>-1/2</sup> )	CPE <sub>2</sub> (Ω.s <sup>n</sup> )	n
<b>Ni/Co-BTC</b>	1.12 × 10 <sup>-6</sup> (1.7%)	1.11 (0.31%)	0.0068 (7.9%)	0.838 (7.2%)	0.063 (3.2%)	-	0.646 (1.2%)	0.84 (0.5%)
<b>Ni/Zn-BTC</b>	9.6 × 10 <sup>-7</sup> (1.9%)	1.17 (0.39%)	0.0068 (4.2%)	0.891 (2.8%)	0.083 (7.7%)	-	0.656 (0.81%)	0.828 (0.42%)
<b>Ni-BTC</b>	8.9 × 10 <sup>-7</sup> (3.9%)	1.19 (0.2%)	0.0067 (2.3%)	0.898 (3.1%)	0.085 (4.5%)	-	0.700 (0.5%)	0.762 (0.4%)
<b>Zn-BTC</b>	9.01 × 10 <sup>-7</sup> (2.03%)	1.12 (0.50%)	0.0065 (4.4%)	0.746 (7.00%)	0.23 (7.04%)	1.81 (2.6%)	-	-
<b>Co-BTC</b>	9.36 × 10 <sup>-7</sup> (1.2%)	1.10 (0.34%)	0.0014 (6.08%)	0.804 (2.25%)	0.38 (2.04%)	1.97 (3.0%)	-	-

L: porous nature of the electrodes, R<sub>s</sub>: electrolyte resistance, R<sub>ct</sub>: charge transfer resistance, CPE1: double layer capacitance, and W and CPE2: diffusion of the ions.



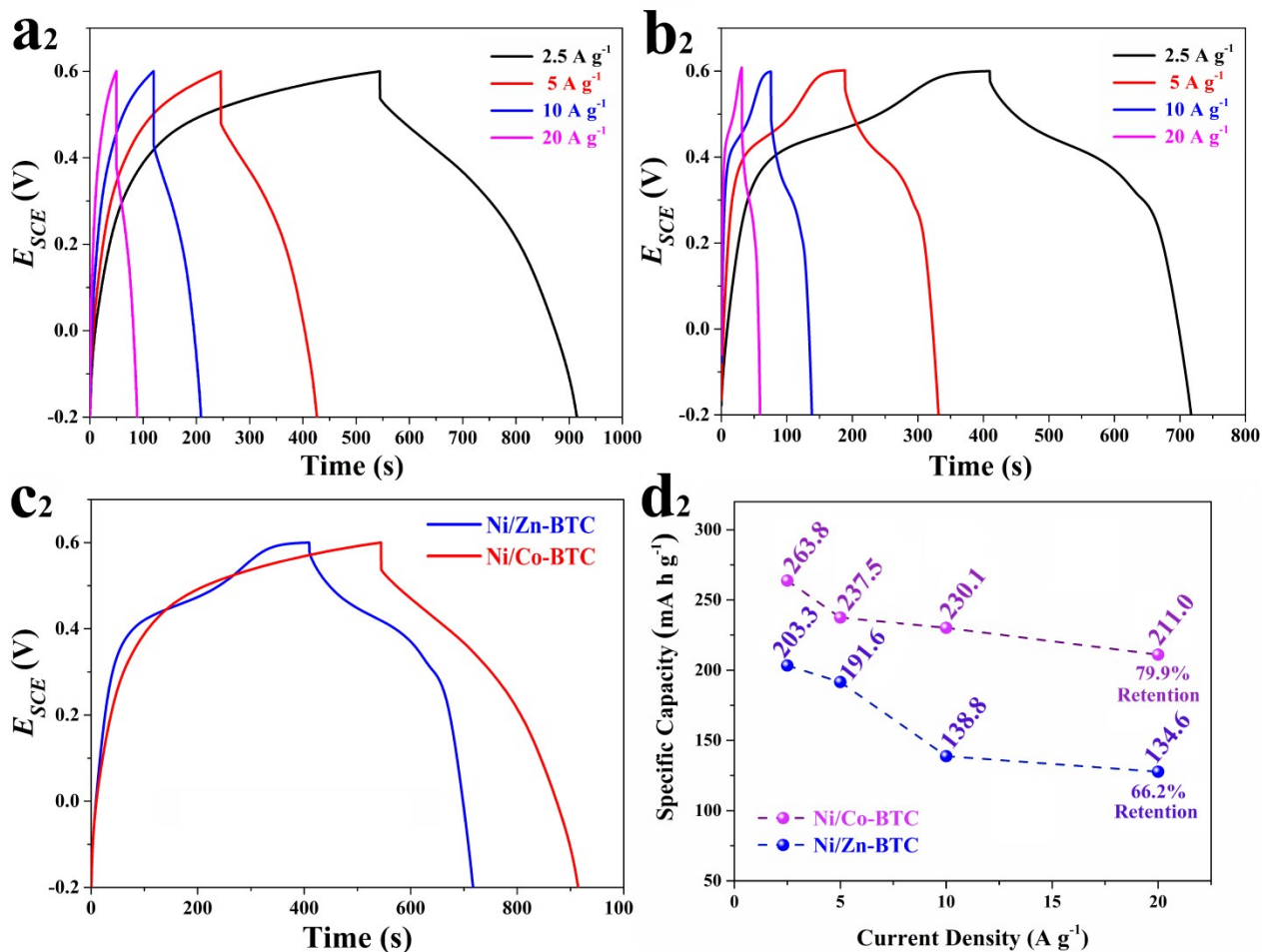


**Figure S10.** (a<sub>1</sub>, and b<sub>1</sub>) three-electrode CVs curves of Ni/Co-BTC and Ni/Zn-BTC electrodes at different scan rates, (c<sub>1</sub>) a comparison between the CV curves of bi-MMOF electrodes at a scan rate of 40 mV s<sup>-1</sup> and, (d<sub>1</sub>) C<sub>s</sub> of bi-MMOF electrodes at various scan rates; (a<sub>2</sub>, and b<sub>2</sub>) three-electrode GCD curves of Ni/Co-BTC and Ni/Zn-BTC electrodes at different currents, (c<sub>2</sub>) a comparison between the GCD curves of bi-MMOF electrodes at 2.5 A g<sup>-1</sup>, and (d<sub>2</sub>) C<sub>s</sub> of bi-MMOF electrodes as a function of current density.

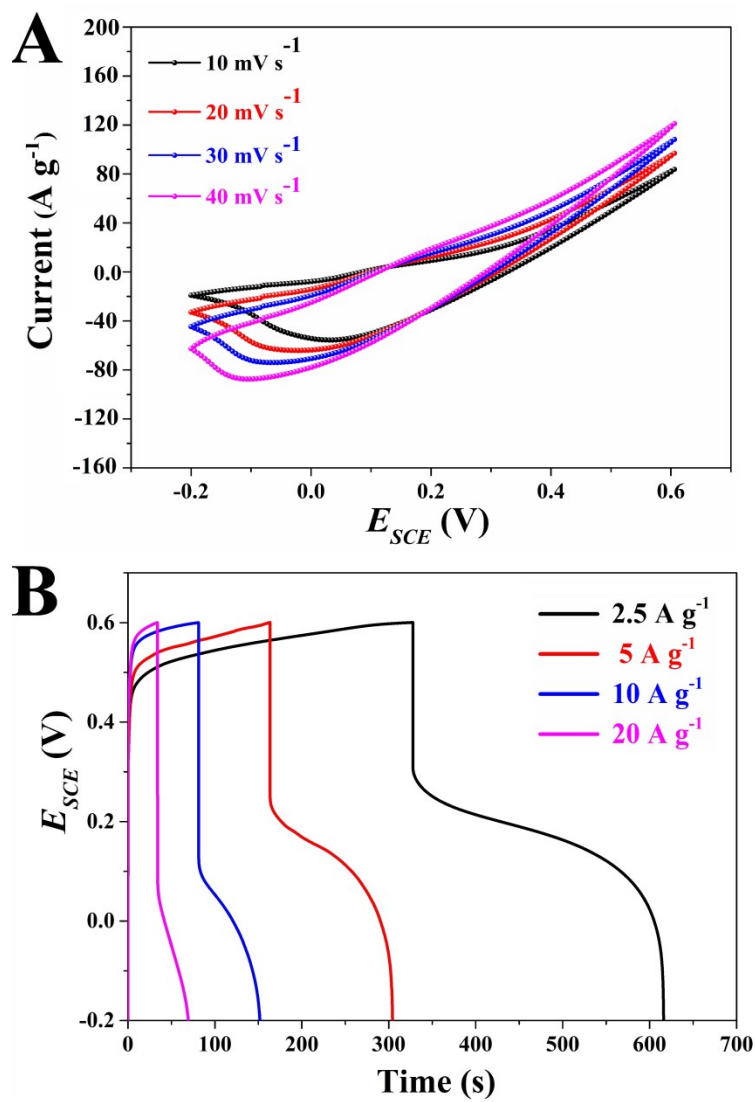


**Figure S11.** (A) Three-electrode CV curves of Ni-MOF at different scan rates, (B) GCD curves of Ni-BTC electrode at different current densities.

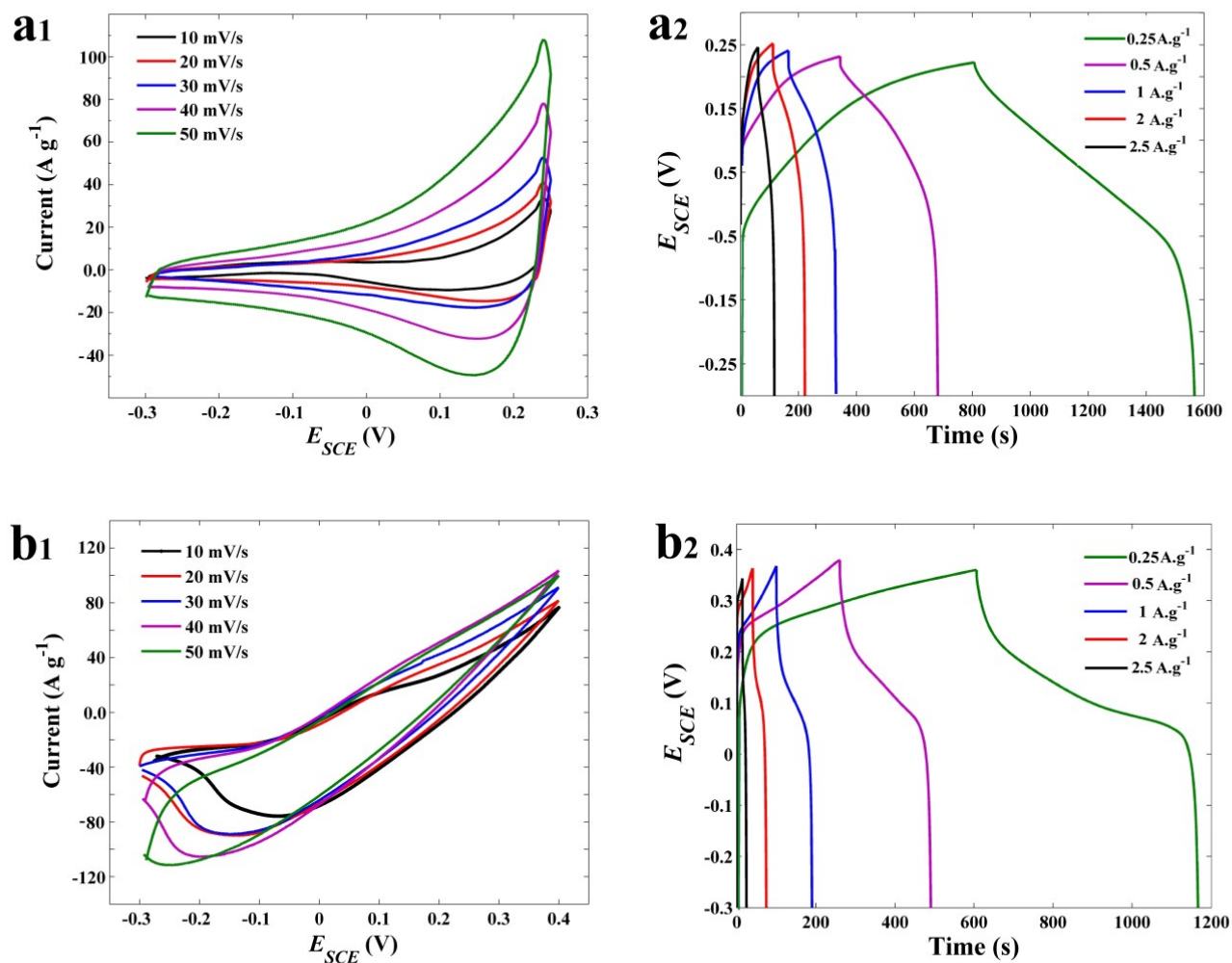


**Figure S12.** (a<sub>1</sub>, and b<sub>1</sub>) Three-electrode CV curves of Zn-MOF and Co-MOF at different scan rates, (a<sub>2</sub>, and b<sub>2</sub>) GCD curves of Zn-BTC and Co-BTC electrodes at different current densities, respectively.

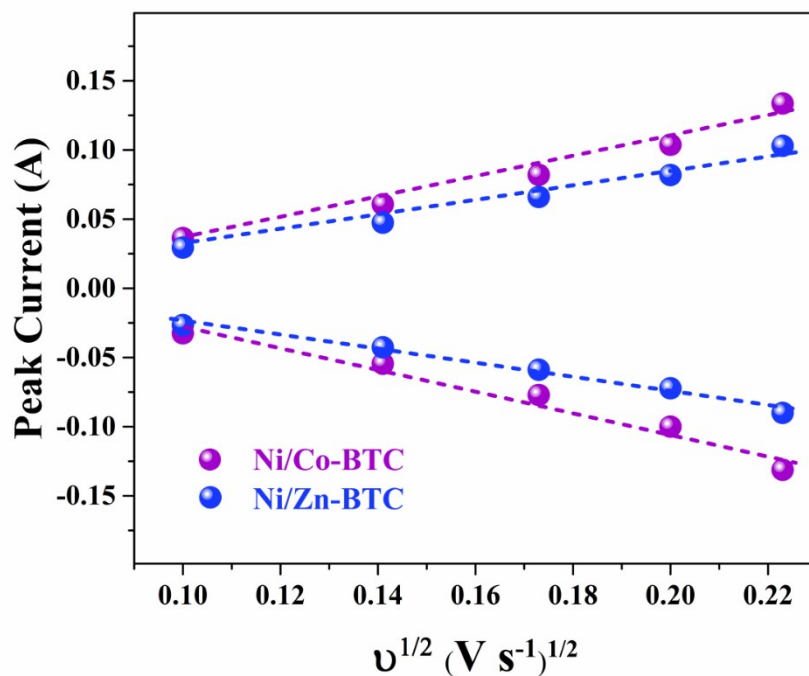


**Figure S13.** The Randles–Sevcik plot of the peak current vs. the square root of the scan rate for Ni/Co-BTC and Ni/Zn-BTC electrodes.

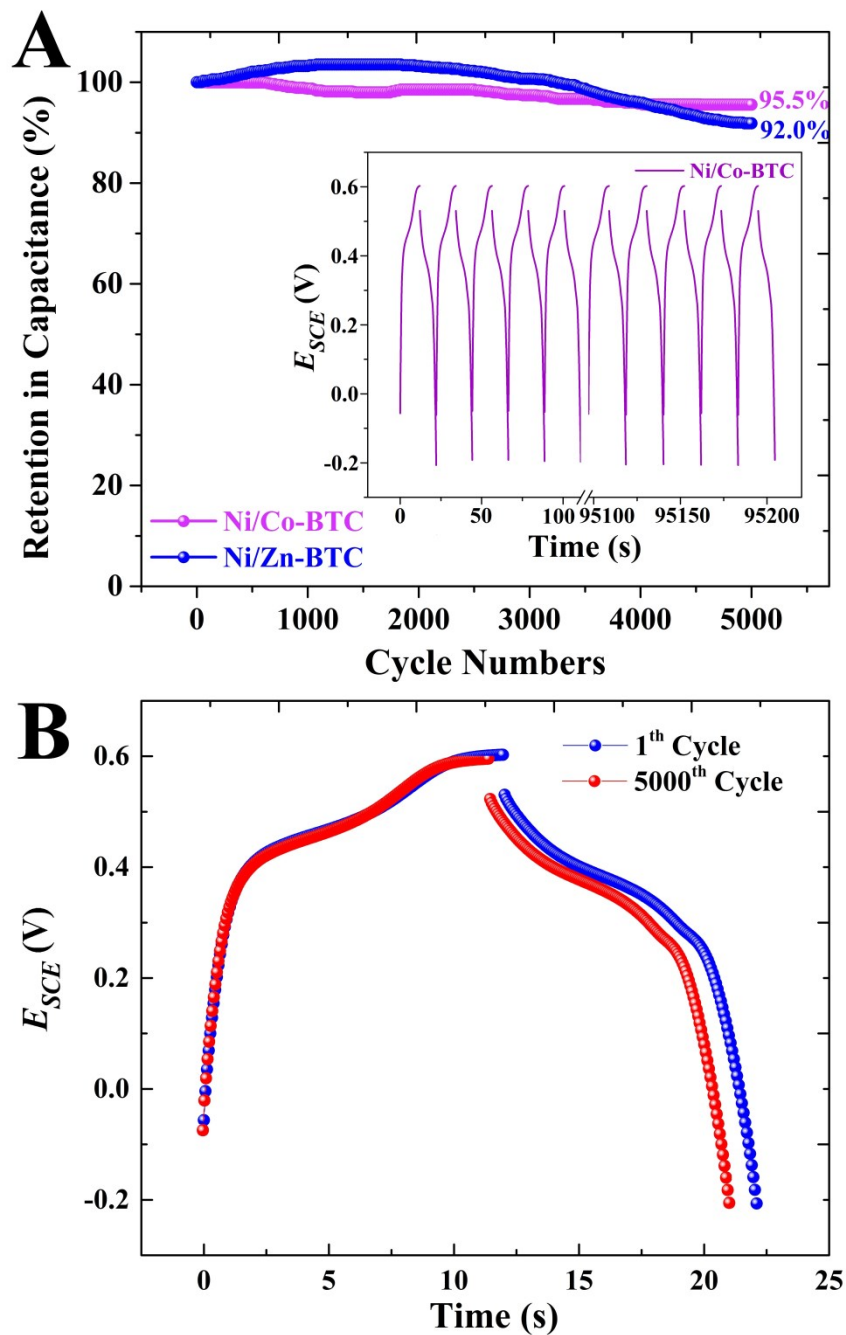


**Figure S14.** (A) Cycle-life stability of the Ni/Co-BTC and Ni/Zn-BTC electrodes at 30.0 A g<sup>-1</sup> for 5000 cycles and (B) comparing the first cycle with the last cycle of capacitance retention test for Ni/Co-BTC electrode.

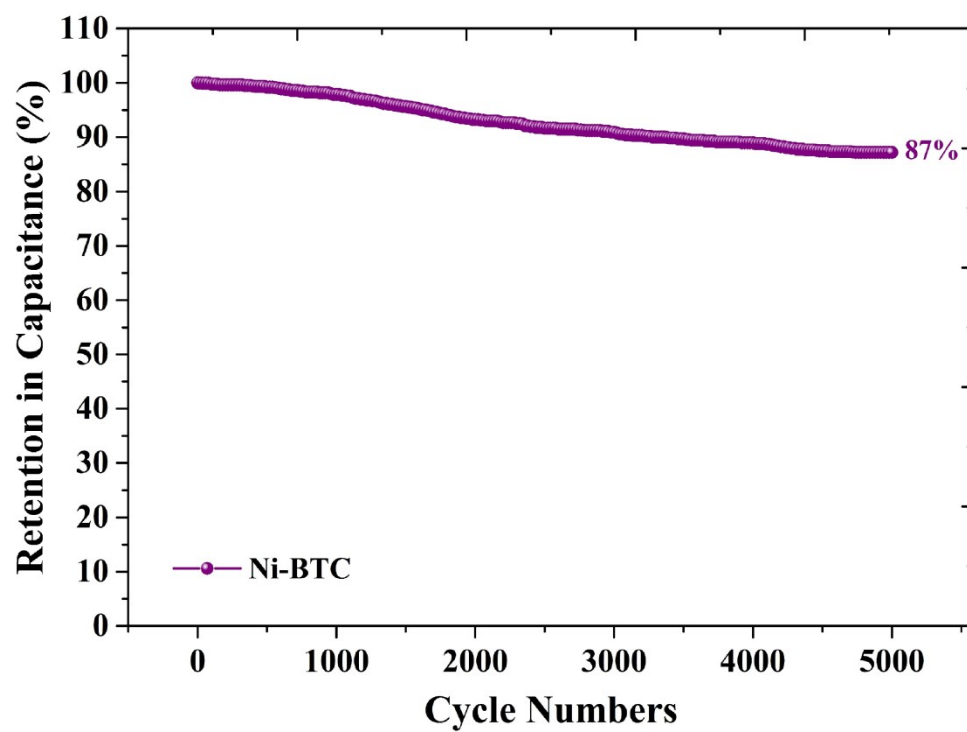


**Figure S15.** Cycle-life stability of the Ni -BTC electrode at 30.0 A g<sup>-1</sup> for 5000 cycles.

**Table S6.** Comparison of the specific capacity of current work to the specific capacity of MOF and MOF-derived material reported in the previous literature.

No.	Electrode material	Electrolyte	Current density (A g <sup>-1</sup> )	Specific capacitance / capacity	Cycle stability	Ref.
1	Ni/Co-MOF	3 M KOH	1	1067 F g <sup>-1</sup>	68.4% capacitance retention after 2500 cycles	12
2	Ni/Co-MOF	3 M KOH	1	1049 F g <sup>-1</sup>	97.4% capacitance retention after 5000 cycles	13
3	NiCo-MOF nanosheet	2 M KOH	1	1202.1 F g <sup>-1</sup>	76.3% capacitance retention after 5000 cycles	14
4	MOF-derived Ni/Co-LDH	6 M KOH	1	1652 F g <sup>-1</sup>	100% capacitance retention after 2000 cycles	15
5	Zn-doped Ni-MOF	6 M KOH	0.25	1620 F g <sup>-1</sup>	92.0% capacitance retention after 3000 cycles	16
6	Ni/Co-MOF	3 M KOH	2.5	263.8 mA h g <sup>-1</sup>	95.5% capacitance retention after 5000 cycles	This Work

**Table S7.** The main performance parameters for the Ni/Co-MOF//Ni/Co-MOF symmetric supercapacitor.

<b>Current density</b> <b>(A g<sup>-1</sup>)</b>	<b>Discharge time</b> <b>(s)</b>	<b>Specific capacitance</b> <b>(F g<sup>-1</sup>)</b>	<b>Energy density</b> <b>(Wh kg<sup>-1</sup>)</b>	<b>Power density</b> <b>(W kg<sup>-1</sup>)</b>
<b>2.5</b>	319	398.7	55.3	624.9
<b>5</b>	144	360	50	1250
<b>10</b>	70	350	48.6	2500
<b>20</b>	31	310	43.05	5000

**Table S8.** The main performance parameters for the Ni/Zn-MOF//Ni/Zn-MOF symmetric supercapacitor.

<b>Current density</b> <b>(A g<sup>-1</sup>)</b>	<b>Discharge time</b> <b>(s)</b>	<b>Specific capacitance</b> <b>(F g<sup>-1</sup>)</b>	<b>Energy density</b> <b>(Wh kg<sup>-1</sup>)</b>	<b>Power density</b> <b>(W kg<sup>-1</sup>)</b>
<b>2.5</b>	165	221.7	26.6	580.45
<b>5</b>	75	187.5	26.04	1250
<b>10</b>	36	180	25	2500
<b>20</b>	17	170	23.6	5000

## References:

1. *MountainsMap® Premium 8*. 2019, Digital Surf, Besançon: France.
2. J. Arjomandi, D. Raoufi and F. Ghamari, *J. Phys. Chem. C*, 2016, **120**, 18055-18065.
3. F. Ghamari, D. Raoufi and J. Arjomandi, *Mater. Chem. Phys.*, 2020, 124051.
4. H. Avireddy, B. W. Byles, D. Pinto, J. M. D. Galindo, J. J. Biendicho, X. Wang, C. Flox, O. Crosnier, T. Brousse, E. Pomerantseva, J. R. Morante and Y. Gogotsi, *Nano Energy*, 2019, **64**, 103961.
5. Y. Jiao, J. Pei, D. Chen, C. Yan, Y. Hu, Q. Zhang and G. Chen, *J. Mater. Chem. A*, 2017, **5**, 1094-1102.
6. S. Stach, Ş. Țălu, S. Abdolghaderi, A. Shafiekhani and J. Bahmani, *Results Phys.*, 2019, **15**, 102731.
7. R. De Levie, *Electrochim. Acta*, 1965, **10**, 113-130.
8. ISO25178-2, *Geometrical product specification (GPS) in Surface texture: Areal - Part 2: Terms, definitions and surface texture parameters*, 2012.
9. V. F. Lvovich, *Impedance spectroscopy: applications to electrochemical and dielectric phenomena*, John Wiley & Sons, 2012.
10. E. Azizi, J. Arjomandi and J. Y. Lee, *Electrochim. Acta*, 2019, **298**, 726-734.
11. T. Pajkossy, *J. Electroanal. Chem. Interf. Electrochem.*, 1991, **300**, 1-11.
12. S. Zhao, L. Zeng, G. Cheng, L. Yu and H. Zeng, *Chin. Chem. Lett.*, 2019, **30**, 605-609.
13. H. Gholipour-Ranjbar, M. Soleimani and H. R. Naderi, *New J. Chem.*, 2016, **40**, 9187-9193.
14. Y. Wang, Y. Liu, H. Wang, W. Liu, Y. Li, J. Zhang, H. Hou and J. Yang, *ACS Appl. Energy Mater.*, 2019, **2**, 2063-2071.
15. Z. Xiao, Y. Mei, S. Yuan, H. Mei, B. Xu, Y. Bao, L. Fan, W. Kang, F. Dai and R. Wang, *ACS Nano*, 2019, **13**, 7024-7030.
16. J. Yang, C. Zheng, P. Xiong, Y. Li and M. Wei, *J. Mater. Chem. A*, 2014, **2**, 19005-19010.